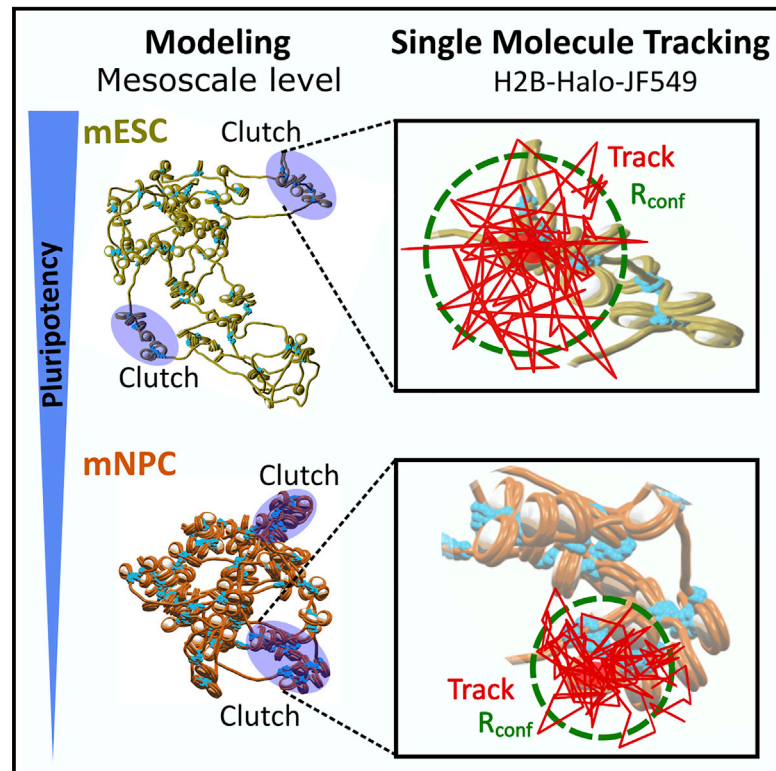


Mesoscale Modeling and Single-Nucleosome Tracking Reveal Remodeling of Clutch Folding and Dynamics in Stem Cell Differentiation

Graphical Abstract



Authors

Pablo Aurelio Gómez-García,
Stephanie Portillo-Ledesma,
Maria Victoria Neguembor, ...,
Tamar Schlick, Maria Pia Cosma,
Melike Lakadamyali

Correspondence

pia.cosma@crg.eu (M.P.C.),
melikel@penmedicine.upenn.edu (M.L.)

In Brief

Gómez-García et al. show that the *Pou5f1* gene folds into nucleosome clutches, with larger clutches in differentiated cells than in stem cells. These clutch changes are accompanied by enhanced hierarchical looping in differentiated cells. H2B dynamics is cell-type specific, correlates with clutch patterns, and is regulated by linker histone H1.

Highlights

- Mesoscale modeling of the *Pou5f1* gene shows cell-type-specific nucleosome clutch patterns
- H2B dynamics is cell-type specific and correlates with nucleosome clutch patterns
- Linker histone H1 plays an important role in regulating H2B dynamics



Article

Mesoscale Modeling and Single-Nucleosome Tracking Reveal Remodeling of Clutch Folding and Dynamics in Stem Cell Differentiation

Pablo Aurelio Gómez-García,^{1,2} Stephanie Portillo-Ledesma,³ Maria Victoria Neguembor,¹ Martina Pesaresi,¹ Walaa Oweis,⁴ Talia Rohrlach,⁴ Stefan Wieser,² Eran Meshorer,^{4,5} Tamar Schlick,^{3,6,7} Maria Pia Cosma,^{1,8,9,10,11,14,*} and Melike Lakadamyali^{12,13,14,15,*}

¹Centre for Genomic Regulation (CRG), The Barcelona Institute of Science and Technology (BIST), 08003 Barcelona, Spain

²Institute of Photonic Sciences (ICFO), The Barcelona Institute of Science and Technology (BIST), Castelldefels, 08860 Barcelona, Spain

³Department of Chemistry, 1021 Silver Center, 100 Washington Square East, New York University, New York, NY 10003, USA

⁴Department of Genetics, The Alexander Silberman Institute of Life Sciences, Faculty of Science, The Hebrew University of Jerusalem, Edmond J. Safra Campus, Givat Ram, Jerusalem 91904, Israel

⁵The Edmond and Lily Safra Center for Brain Sciences (ELSC), The Hebrew University of Jerusalem, Edmond J. Safra Campus, Givat Ram, Jerusalem 91904, Israel

⁶Courant Institute of Mathematical Sciences, 251 Mercer Street, New York University, New York, NY 10012, USA

⁷NYU-ECNU Center for Computational Chemistry at New York University Shanghai, 340 Geography Building, 3663 North Zhongshan Road, Shanghai 3663, China

⁸Universitat Pompeu Fabra (UPF), Dr Aiguader 88, 08003 Barcelona, Spain

⁹Institució Catalana de Recerca i Estudis Avançats (ICREA), Pg. Lluís Companys 23, 08010 Barcelona, Spain

¹⁰Bioland Laboratory, Guangzhou Regenerative Medicine and Health Guangdong Laboratory, Guangzhou 510005, China

¹¹CAS Key Laboratory of Regenerative Biology, Guangdong Provincial Key Laboratory of Stem Cell and Regenerative Medicine, Guangzhou Institutes of Biomedicine and Health, Chinese Academy of Sciences, Guangzhou 510530, China

¹²Perelman School of Medicine, Department of Physiology, University of Pennsylvania, Clinical Research Building, 415 Curie Boulevard, Philadelphia, PA 19104, USA

¹³Perelman School of Medicine, Department of Cell and Developmental Biology, University of Pennsylvania, Biomedical Research Building, 421 Curie Boulevard, Philadelphia, PA 19104, USA

¹⁴These authors contributed equally

¹⁵Lead Contact

*Correspondence: pia.cosma@crg.eu (M.P.C.), melikel@penmedicine.upenn.edu (M.L.)

<https://doi.org/10.1016/j.celrep.2020.108614>

SUMMARY

Nucleosomes form heterogeneous groups *in vivo*, named clutches. Clutches are smaller and less dense in mouse embryonic stem cells (ESCs) compared to neural progenitor cells (NPCs). Using coarse-grained modeling of the pluripotency *Pou5f1* gene, we show that the genome-wide clutch differences between ESCs and NPCs can be reproduced at a single gene locus. Larger clutch formation in NPCs is associated with changes in the compaction and internucleosome contact probability of the *Pou5f1* fiber. Using single-molecule tracking (SMT), we further show that the core histone protein H2B is dynamic, and its local mobility relates to the structural features of the chromatin fiber. H2B is less stable and explores larger areas in ESCs compared to NPCs. The amount of linker histone H1 critically affects local H2B dynamics. Our results have important implications for how nucleosome organization and H2B dynamics contribute to regulate gene activity and cell identity.

INTRODUCTION

Genome organization and dynamics play an important role in regulating gene expression. Several recent studies, including super-resolution imaging of nucleosomes and electron tomography imaging of DNA, highlighted that chromatin is disordered and heterogeneous groups of nucleosomes with a varying range of nucleosome densities are present in folded chromatin (Ou et al., 2017; Ricci et al., 2015). In super-resolution images, nucleosome groups (named clutches) were further clustered into

larger domains (clutch domains) in the size range of hundreds of nanometers in length scale (Lakadamyali and Cosma, 2020; Otterstrom et al., 2019; Ricci et al., 2015). These results shed new light onto the organization of chromatin fiber at the 10–100 nm length scales. Assembly of nucleosomes into clutches, the compaction level of nucleosomes within clutches, and the assembly of clutches into clutch domains can limit accessibility of DNA to regulatory proteins and polymerases. Hence, these structural features must be dynamically regulated as genes turn on and off in specific cell types.



Indeed, fluorescence recovery after photobleaching (FRAP) analysis and single-molecule tracking (SMT) of histone proteins, as well as tracking of individual genomic loci within the nucleus, demonstrated that chromatin is highly dynamic. Individual genomic loci diffuse within a confined space in the nucleus (Neu-guembor et al., 2018; Shaban et al., 2018; Shukron et al., 2019), and this mobility correlates with the transcriptional activity of some genomic regions such as enhancers (Chen et al., 2018; Shukron et al., 2019). In some cases, genomic loci dynamically reposition over large distances, for example by relocating from the nuclear periphery to the nuclear interior upon activation (Chuang et al., 2006; Neumann et al., 2012). While FRAP analysis showed that nucleosomes are highly stable and turn over slowly (Kimura and Cook, 2001), tracking of tagged histone proteins showed that histones also explore their local environment dynamically (Lerner et al., 2020; Nagashima et al., 2019; Nozaki et al., 2017). Live-cell super-resolution imaging showed that chromatin domains that are hundreds of nanometers in size are also mobile (Boettiger et al., 2016; Nozaki et al., 2017, 2018). In addition to chromatin fluidity, several studies showed that architectural proteins are also highly dynamic inside the nucleus (Hansen et al., 2017; Higashi et al., 2007). In particular, the dynamics of architectural proteins like H1 and HP1 increase in embryonic stem cells (ESCs), as shown by FRAP and SMT (Bryan et al., 2017; Meshorer et al., 2006). Based in part on these FRAP studies, it has been suggested that ESC chromatin is hyperdynamic and depleted of heterochromatin (Schlesinger and Meshorer, 2019). However, how these dynamic chromatin entities spanning multiple length scales, from individual nucleosomes to large genomic loci, relate to each other and the associated mechanisms of their folding and dynamics remain unknown due to the limitations of previous methods used to analyze chromatin dynamics. In particular, previous FRAP studies (Hansen et al., 2017; Higashi et al., 2007; Kimura, 2005; Kimura and Cook, 2001; Meshorer et al., 2006; Rhodes et al., 2017) reported bulk histone turnover within diffraction limited volumes ($\sim 300 \times 300 \times 500 \text{ nm}^3$), and these studies were not able to assess fast dynamics or dynamics of individual histones (Meshorer et al., 2006). Live-cell super-resolution imaging has thus been used to investigate the dynamics of sub-diffraction-sized chromatin domains (100–200 nm in size) (Nozaki et al., 2017). While the dynamics of individual histones was also tracked and qualitatively compared to the dynamics of these larger domains, the use of a dim fluorescent protein that is prone to rapid photobleaching compromised the spatial resolution attained in these studies, inhibiting the analysis of nucleosome clutches or small histone displacements. Hence, the analysis was mainly limited to large chromatin domains rather than individual histones. Overall, how individual histones move within the chromatin fiber, their dwell time within chromatin, how these dynamic parameters change in different cell types, and the underlying mechanisms that influence local histone mobility remain open questions.

Super-resolution imaging showed that nucleosome clutch size is cell-type specific and that ESCs have smaller, less compact clutches compared to differentiated neural progenitor cells (NPCs) (Ricci et al., 2015). We further noted that nucleosome clutch size and compaction depends on the amount of linker histone H1 (Ricci et al., 2015), as well as the amount of acetylation

on histone tails (Otterstrom et al., 2019), suggesting that linker histones and histone post-translational modifications play a role in organizing nucleosomes into clutches. How nucleosome clutch organization in fixed stem and somatic cells correlates with histone dynamics in live cells remains an open question.

Here, to address these questions and analyze the organizational patterns of nucleosomes and dynamics of histones within clutches in mouse ESCs and NPCs, we combined coarse-grained mesoscale models of kilobase-range nucleosome fibers and SMT of individual histones. Mesoscale models of chromatin fibers of the pluripotency gene *Pou5f1*, which expresses the pluripotency factor OCT4, revealed the presence of nucleosome clusters compatible with the nucleosome clutches previously observed genome-wide in super-resolution images. The previously observed global changes in clutch size and compaction upon differentiation (Otterstrom et al., 2019; Ricci et al., 2015) were reproduced in the models at the level of a single pluripotency gene locus. These modeling results further suggest that the *Pou5f1* fiber undergoes overall compaction in NPCs, especially in regions surrounding the *Pou5f1* gene and its super enhancer. Hierarchical looping, corresponding to stacks in space of hairpin loop structures (Grigoryev et al., 2016), is further enhanced in NPC *Pou5f1* fibers, explaining the formation of larger clutches. The nucleosomes within clutches maintain a configuration most compatible with zigzag geometry in both ESCs and NPCs irrespective of clutch size.

To determine how differences in the structural features of clutches in different cell types relate to the dynamic properties of histones, we further used fast and slow SMT to visualize individual histones with bright and photostable JaneliaFluor dyes using the Halo-tagging strategy. We show that histone H2B is dynamic *in vivo* and explores its local environment within the chromatin fiber. Importantly, we show that this local H2B mobility takes place at fast timescales (tens of milliseconds) and is distinct from the mobility of larger chromatin domains containing hundreds of nucleosomes, which remain stable in these timescales. The smaller and more open clutches of ESCs compared to the larger and more compacted clutches of NPCs correlate with local H2B dynamics and residence times observed in the two cell types. To further explore the mechanisms underlying these cell-type-specific differences in the fast local mobility of histones as well as their residence times within chromatin, we tracked nucleosomes in a cell line that lacks three isoforms of the linker histone H1. We show that histone residence times within chromatin and the extent of the fast local histone mobility within the chromatin fiber are both dependent on the amount of linker histone H1. These results offer a rich picture of nucleosome dynamics and link nucleosome dynamics to structural differences in nucleosome organization in different cell types.

RESULTS

Mesoscale Modeling of the *Pou5f1* Pluripotency Gene Reveals a Chromatin Fiber Conformation Composed of Nucleosome Clusters Whose Organization and Compaction Change upon Differentiation

Recently, using super-resolution microscopy, we showed that nucleosome clutches contain a median number of ~ 6

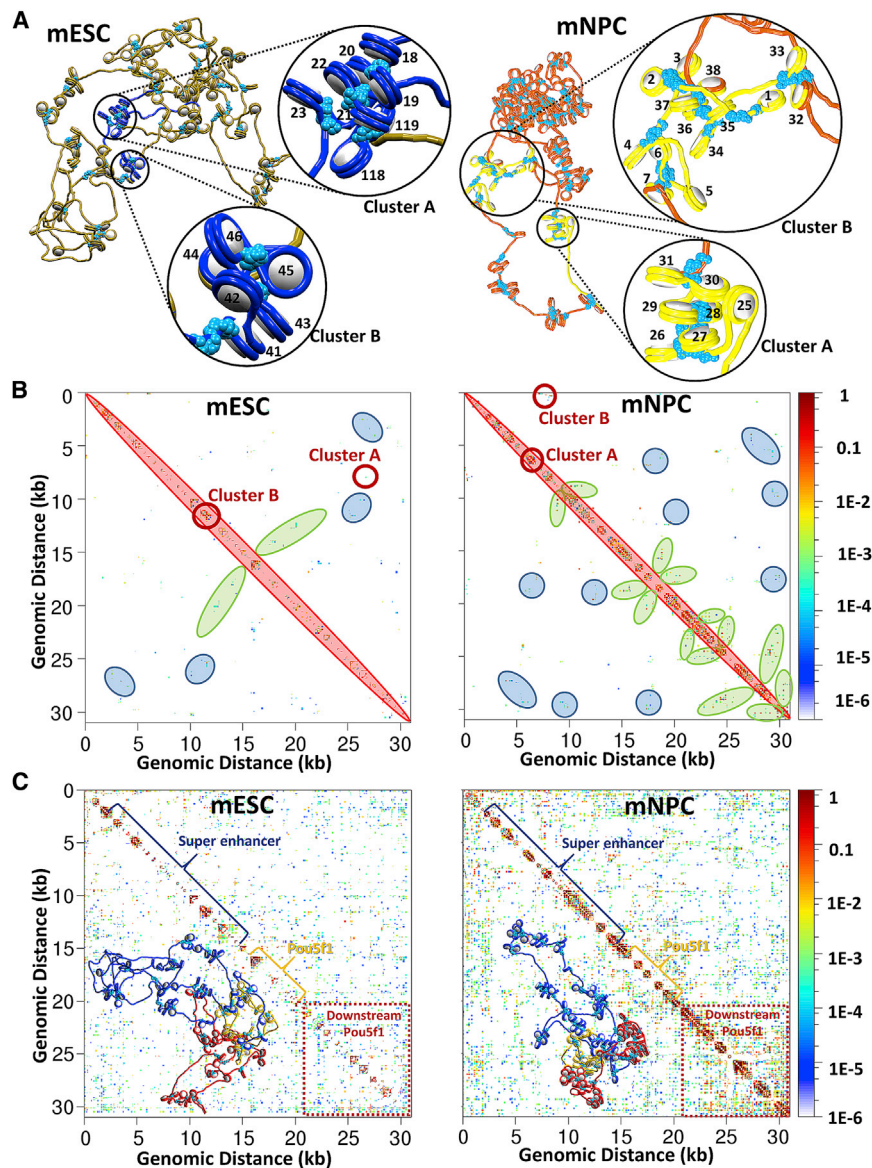


Figure 1. Nucleosome Architecture of the *Pou5f1* Pluripotency Region Revealed by Computational Modeling

(A) Representative equilibrated structures of chromatin fibers corresponding to the *Pou5f1* pluripotency region in mESCs (left) and mNPCs (right) obtained from mesoscale modeling are shown. Zooms show the nucleosome clusters obtained from DBSCAN analysis of the 3D chromatin fibers. The numbers correspond to the identity of the nucleosomes based on their linear sequence along the *Pou5f1* region.

(B) Internucleosome contact probability maps for the fibers shown in (A). Hierarchical folding (indicated in blue) and hairpin folding (indicated in green) revealed in the internucleosome contact matrices for representative mESC and mNPC chromatin fibers. These structural features were previously defined (Grigoryev et al., 2016) and are determined based on the shape of the nucleosome contact density in the map (STAR Methods). In addition to these previously defined features, density corresponding to nucleosome clusters are also detected in the maps (red circles). Matrices are normalized by the maximal number of contacts seen throughout the trajectory. The matrix densities are 0.007 and 0.024 for mESCs and mNPCs, respectively.

(C) Internucleosome contact probability matrices for the 30 trajectory ensemble per condition. Contact probability matrices were obtained by normalizing contact maps by the maximum number of contacts across each trajectory, for each system, and summing all contacts. One representative fiber for each system is shown with yellow nucleosome perimeters for the *Pou5f1* region, blue for the super enhancer region, and red for the downstream *Pou5f1* region. The dashed red box in the mNPC matrix corresponds to the region downstream of *Pou5f1*. The matrix densities are 0.0546 and 0.1322 for the ensemble of mESCs and mNPCs, respectively.

nucleosomes in somatic cells (Ricci et al., 2015) corresponding to a genomic length scale of a few kilobases. We further showed that the size of the nucleosome clutches inversely correlates with the pluripotency grade of mouse ESCs (mESCs), as well as human induced pluripotent stem cells (hiPSCs) (Ricci et al., 2015). In particular, upon *in vitro* differentiation of mESCs into mouse NPCs (mNPCs), clutch size increases (Ricci et al., 2015). In addition, mutant mESCs lacking three isoforms of the linker histone H1 (H1tKO) (Fan et al., 2005) have smaller nucleosome clutches compared to wild-type mESCs (Ricci et al., 2015). These results suggest that nucleosome clutches correlate well with the open or closed state of the chromatin fiber, and they are remodeled in cellular reprogramming and differentiation.

To gain further insights into the chromatin remodeling of mESCs during differentiation (Otterstrom et al., 2019; Ricci et al., 2015), we simulated chromatin fibers typical of mESCs

and mNPCs (Figures 1 and S1) using our nucleosome-resolution chromatin mesoscale model (Bascom et al., 2016). The model applied to the study of many biological problems, including, most recently, gene folding (Bascom et al., 2019), combines nucleosomes, histone core tails, linker DNA, and linker histones by coarse-grained units at different levels of resolution to create oligonucleosome fibers (Collepardo-Guevara and Schlick, 2014; Perišić et al., 2010) (Figure S1A). Fiber configurations are sampled by Monte Carlo (MC) simulations that survey and approach equilibrium conformations (Bascom et al., 2016; Collepardo-Guevara and Schlick, 2014; Perišić et al., 2010) (STAR Methods).

To define chromatin fibers relevant to stem cell pluripotency and differentiation, we selected a specific genomic region of ~30 kbp that includes an important pluripotency gene, *Pou5f1*, active in mESCs but silenced in mNPCs (Zeineddine et al.,

2014). We confirmed that the expression level of the *Pou5f1* gene was downregulated by 7-fold upon differentiation of mESCs to mNPCs, along with expected downregulation of other pluripotency genes like *Nanog* and upregulation of neuronal genes like *Sox1* and *Nestin* (Figure S1B). We sought to capture the measured changes in *Pou5f1* gene expression by differences in clutch patterns and overall compaction. We expected mESC fibers to form smaller clutches compared to mNPC fibers based on previous super-resolution data. We used publicly available MNase-seq data of mESCs and mNPCs (Mieczkowski et al., 2016) to position the nucleosomes, define the H1 to nucleosome ratio (Woodcock et al., 2006), and specify the amount of histone tail acetylation in the two cell types (Meshorer et al., 2006) (STAR Methods; Figures S1C–S1E). We expect these parameters to be important for organizing gene structure (Bascom et al., 2016, 2019; Bascom and Schlick, 2018), clutch organization, and DNA compaction (Otterstrom et al., 2019; Ricci et al., 2015) based on previous modeling and experimental results from super-resolution. Specially, the nucleosome positions obtained from the MNase-seq data (Mieczkowski et al., 2016) determine the DNA linker lengths and the nucleosome-free regions (NFRs) (Figures S1D and S1E), key factors affecting chromatin. To incorporate realistic linker histone H1 densities, we used linker histone to nucleosome ratios of 0.5 and 0.8 for mESCs and mNPCs, respectively, as reported previously (Woodcock et al., 2006). Histone tail acetylation patterns were assigned as determined previously (Meshorer et al., 2006; Roh et al., 2007), with overall levels of 15% and 10% for mESCs and mNPCs, respectively, based on immunofluorescence measurements (STAR Methods; Figure S1C; Table S1).

Both the mESC and mNPC systems were simulated by 30 independent trajectories of 80 million MC steps each (Video S1). Visual inspection of the resulting chromatin fibers revealed a significant difference in global fiber shape for the different cell types; mNPC fibers were more compact than mESC fibers (Figure 1A). Quantitative analysis (STAR Methods) confirmed higher sedimentation coefficients (Figure S2A), smaller radii of gyration (Figure S2B), and volume (Figure S2C) for the mNPC fibers compared to the mESC fibers. These quantitative results are consistent with the visually more compact mNPC fibers, which revealed nucleosomes grouped together into heterogeneous clusters resembling nucleosome clutches previously described in super-resolution images. To confirm the visual inspection quantitatively and gain a detailed understanding of nucleosome patterns inside the clusters, we further analyzed the 3D fibers using density-based spatial clustering of applications with noise (DBSCAN) (Ester et al., 1996). This analysis revealed nucleosome clusters consisting on average of 6 and 18 nucleosomes per cluster in mESCs and mNPCs, respectively (Figure S2D). The nucleosome packing ratio within the clusters was also significantly higher in mNPCs compared to mESCs (Figure S2E). Finally, mNPC fibers contained fewer nucleosome clusters compared to mESC fibers (Figure S2F), consistent with the nucleosome clusters becoming larger in mNPCs.

Internucleosome contact probability matrices for the two selected fibers shown in Figure 1A further revealed increased nucleosome contacts in mNPCs compared to mESCs (average matrix density of 0.007 and 0.024 for mESCs and mNPCs,

respectively) (Figure 1B), consistent with the increased fiber compaction and larger nucleosome clusters of mNPCs. Interestingly, distant nucleosomes appear to interact within the larger clusters (see cluster A of mESCs and cluster B of mNPCs in Figure 1A). Features consistent with nucleosome clusters and folding motifs such as hairpin and hierarchical loops are evident in the nucleosome contact matrices (Figure 1B); hierarchical loops correspond to stacks of hairpin loops (STAR Methods) (Grigoryev et al., 2016). The hairpin and hierarchical loops are evident from the contact maps as regions of medium-range contacts perpendicular to the main diagonal (hairpins) and regions of long-range contacts parallel to the main diagonal (hierarchical looping) (Figure S2G). These features are enhanced in mNPCs compared to mESCs and likely explain the formation of larger clutches upon differentiation by increased contact of distant nucleosomes upon folding. By further generating averaged internucleosome contact probability matrices for all the 30 fibers per condition (Figure 1c), we further confirmed the presence of enhanced nucleosome contact frequency in mNPC fibers (average matrix density of 0.0546 and 0.1322 for the ensemble of mESCs and mNPCs, respectively). Interestingly, the highest enhancement in contact probability was observed in the region downstream of the *Pou5f1* gene/super-enhancer region (dashed red box in Figure 1C), corresponding to a higher-level of compaction for this downstream region. Finally, the distance between nucleosomes dimers as well as the triplet and dihedral angle of bonded (i.e., consecutive) nucleosomes (Figures S2H and S2I) were most consistent with a zigzag geometry in both cell types. This feature underscores the prevalence of the zigzag secondary structure topology (Grigoryev et al., 2016).

Nucleosome Clusters of *Pou5f1* Fibers in the Mesoscale Models Are Compatible with Nucleosome Clutches Observed in Super-resolution Genome-wide

DBSCAN analysis of the modeled 3D fibers is consistent with previous super-resolution data that revealed that nucleosomes form heterogeneous clutches *in vivo*. However, given that the super-resolution images have lower resolution and are genome-wide with no sequence specificity compared to the modeled fibers, to directly relate the model fiber configurations to previous experimental super-resolution data, we simulated super-resolution images from the modeled fibers using the simulation package SuReSim (Venkataramani et al., 2016) (STAR Methods; Figure 2A). Since the chromatin fiber generated by the model is 3D but our super-resolution images are 2D, we performed 1,000 2D random projections on each resulting super-resolution localization list (STAR Methods; Figure 2A). We applied a distance-based clustering algorithm (Ricci et al., 2015) to group the fluorophore positions in the simulated super-resolution images and segment nucleosome clutches as previously described (STAR Methods; Figure 2A). This analysis confirmed the presence of nucleosome clutches in the 2D projections of the simulated super-resolution images from the 3D model (Figures 2A, S3A, and S3B). We compared the identity of the nucleosomes in the segmented clutches to that of 3D clusters determined by DBSCAN analysis for clusters A and B in the example simulated fiber shown in Figure 1A. As expected, depending on the 2D projection, the clutches contained all or only a subset of the

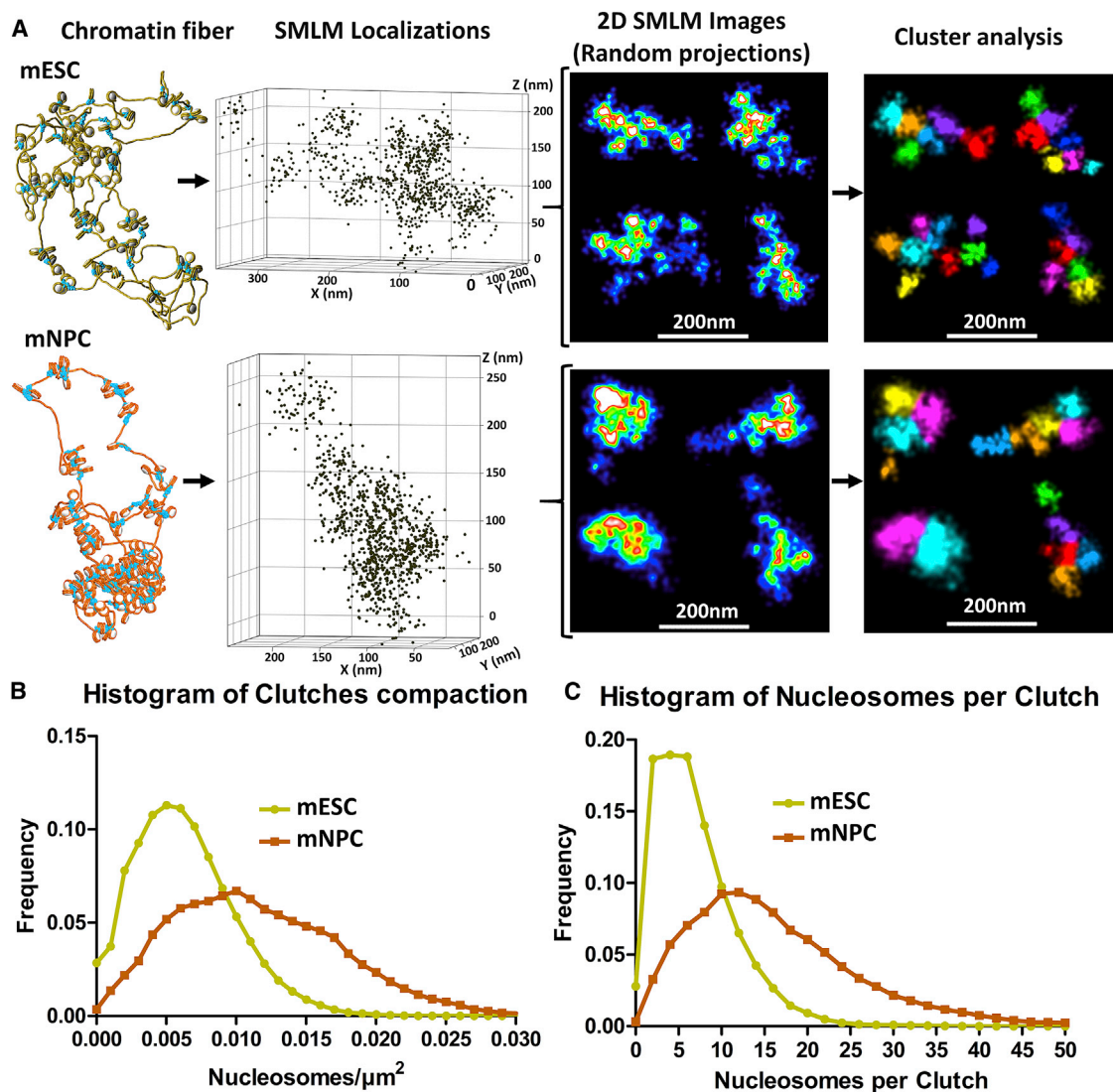


Figure 2. Mesoscale Modeling of Chromatin Fibers Recapitulates Super-resolution Images of Nucleosomes

(A) Workflow showing the procedure for generating super-resolution images from a given computational chromatin fiber. First, the nucleosome positions within the 3D fibers (chromatin fiber) are converted into localized x, y, and z positions of nucleosomes (referred to as single-molecule localization microscopy [SMLM] localizations) with SuReSim. Then the localizations are rotated 1,000 times in 3D by randomly picking an angle and axis of rotation to obtain random 2D projections. Finally, the 3D coordinates of the localizations are projected in a 2D slice with a maximum depth of 400 nm. The 2D localizations are then rendered as a super-resolution image (SMLM image) by representing each localization as a Gaussian with a fixed width of 9 nm. The color coding corresponds to the density of localizations. Finally, cluster analysis is performed to segment the localizations based on their spatial proximity. Each cluster is pseudo-color-coded with a different color.

(B and C) Histogram of nucleosome packing density (i.e., number of nucleosomes per clutch area). (B) Histogram of the number of nucleosomes per clutch. (C) Computed from the cluster analysis of the simulated super-resolution images of Pou5f1 in mESCs (yellow) and mNPCs (orange).

nucleosomes in the 3D clusters (Figures S3A–S3C). Similarly, in some 2D projections, nucleosomes found within different 3D clusters could merge into the same clutch (Figure S3C).

The compaction level of nucleosomes within clutches ($6.2 \times 10^{-3} \pm 3.5 \times 10^{-3}$ nucleosomes/ μm^2 for mESCs and $11.5 \times 10^{-3} \pm 6 \times 10^{-3}$ nucleosomes/ μm^2 for mNPCs) (Figure 1B) and the number of nucleosomes per clutch (6.4 ± 4.7 nucleosomes/clutch in mESCs compared to 16.4 ± 11.3 nucleosomes/clutch in mNPCs) (Figure 2C) were higher in mNPCs

compared to mESCs (Otterstrom et al., 2019; Ricci et al., 2015). Despite the above-mentioned differences between the 3D model and the simulated images, remarkably, the number of nucleosomes per clutch in the two cell types was in close agreement with the DBSCAN results obtained from directly analyzing the 3D fibers at higher resolution (Figure S2D). Previous super-resolution experimental data showed a median number of ~ 3 and ~ 6 nucleosomes per clutch averaged globally over the entire chromatin of mESCs and mNPCs, respectively. The

number of nucleosomes per clutch is lower in the experimental data compared to the model, which may reflect differences in the global clutch configuration versus the local *Pou5f1* gene clutch configuration. The experimental data may also potentially underestimate the number of nucleosomes per clutch due to labeling inefficiencies, particularly in more compact regions. Nonetheless, the comparison of experimental data and simulated images to the model revealed that the global changes in clutch conformation of mESCs and mNPCs are representative of specific changes to the clutch conformation of a model pluripotency gene like *Pou5f1*. In fact, these differences in clutch conformation are likely even more prominent in specific genomic regions that change their expression level upon differentiation compared to genome-wide differences in clutches. In addition to differences in the number and compaction of nucleosomes in clutches, significant differences were also observed for the number of clutches per fiber (Figure S3D), the clutch area (Figure S3E), and the nearest-neighbor distance between clutches (Figure S3F) in the two cell types.

Overall, our results show a heterogeneous chromatin fiber conformation both globally and at the level of specific pluripotency genes, manifested as heterogeneous groups of nucleosome clutches. In addition, we reveal the presence of folding motifs like hierarchical looping, which are cell-type specific and dynamically change upon cell differentiation.

H2B Residence Time within Chromatin Increases in Differentiation

Given our super-resolution and modeling results that reveal dramatic structural reorganization of the chromatin fiber both globally and at specific genes during differentiation, we wanted to explore how the local dynamics of individual histones forming the nucleosomes within clutches change upon differentiation and how these dynamics relate to the structural changes observed. We thus generated mESCs or mESCs-H1tKO (triple knockout of the linker histone H1) (Fan et al., 2005) cell lines stably expressing H2B fused to Halo tag at low levels. We confirmed using western blot analysis that the Halo-tagged H2B is fully incorporated into chromatin bound fraction in these cell lines (Figure S4A). Indeed, western blot showed that Halo-H2B in mESCs was present only in the chromatin-bound fraction and not in the nuclear soluble or cytoplasmic fraction (Figure S4A). We next used a 10-pM concentration of the bright and photostable Janelia Fluor 549 (JF549)-tagged Halo ligand to sparsely label H2B molecules within the nucleus (Figures S4B and S4C). Using SMT, we measured H2B dynamics in mESCs, mESCs-H1tKO or mNPCs that were obtained upon differentiation of the Halo-H2B expressing mESCs with retinoic acid treatment (STAR Methods). Importantly, we used low light illumination levels throughout the experiments (STAR Methods) and avoided a pre-photobleaching step typically used in SMT (Chen et al., 2014) to not compromise cell viability. Further, by labeling DNA with Hoechst and taking a snapshot of the nuclei before and after SMT, we ensured that the nuclei were stable during the imaging process.

First, using slow SMT, we determined the residence times of H2B in mESCs, mESCs-H1tKO, and mNPCs (STAR Methods). As a control, we also measured residence times in fixed cells

and used it as a normalization for the residence times measured in living cells. The positions of tracked molecules were distributed randomly within the nuclei, and hence, there was no spatial bias in the sampling of H2B molecules (Figure S4C). Further, the signal to noise ratio of the localized H2B-Halo molecules (Figure S4D) and the photobleaching kinetics (Figure S4E) were comparable among the different cell types and in fixed cells. H2B residence time in living cells was lower in all three cell types compared to fixed cells, suggesting that H2B is dynamic and likely turns over *in vivo* (Figure 3a). H2B residence time was shortest in mESCs-H1tKO and progressively increased in wild-type mESCs and mNPCs, suggesting that H2B is more stable in differentiated cells (Figure 3A). The H1 to H2B ratio is higher in mNPCs compared to mESCs (Woodcock et al., 2006); as a result, H1 may play a role in stabilizing H2B and increasing its residence time within chromatin. Knocking out three isoforms of the linker histone had a significant effect on H2B residence time (Figure 3A), suggesting that the amount of H1 is an important factor for stabilizing and increasing H2B's residence time within chromatin.

H2B Exhibits More Confined Mobility within Chromatin upon Differentiation

To characterize H2B mobility at faster timescales, we carried out fast SMT (STAR Methods) and detected three different motion types in the H2B trajectories (Figures 3B and S4F): (1) confined motion, likely corresponding to H2B stably incorporated into nucleosomes; (2) Brownian diffusion, likely corresponding to free H2B not incorporated into nucleosomes; and (3) switching behavior between confined motion and Brownian diffusion (butterfly motion), likely corresponding to transient destabilization of the nucleosomes (Izeddin et al., 2014; Monnier et al., 2015; Shen et al., 2017). The majority of H2B belonged to the first category in all three cell types (Figure 3B), further supporting the notion that H2B is mainly chromatin bound. As a control, we also tracked transcription factors, including OCT4 and CCCTC-binding factor (CTCF) and, as expected, we find them to be more dynamic compared to H2B (Figures S5A–S5C). To determine the extent of local H2B mobility, we analyzed the radius of confinement of H2B from the sub-population of H2B molecules that exhibited confined motion. This analysis showed a radius of confinement of 50 nm in fixed cells, which corresponds to the localization precision of our measurements (Figure 3C). In living cells, the radius of confinement was larger compared to fixed cells for all cell types (Figure 3C), underscoring the dynamic nature of H2B during its residence time within chromatin. The radius of confinement was largest in mESCs-H1tKO (157 ± 6 nm), lacking linker histone, and progressively decreased in mESCs (115 ± 3 nm) and mNPCs (82 ± 1.5 nm) (Figure 3C). We observed large differences in the radius of confinement between mESCs-H1tKO and wild-type mESCs (Figure 3C), suggesting that the local dynamics of chromatin bound H2B is mostly constrained by the presence of linker histone H1.

To further confirm that these dynamics correspond to local motion of H2B within the chromatin fiber, rather than the motion of large chromatin domains, we tracked telomeres and centromeres using SMT (Figure 4). Telomeres are at the ends of chromosomes and can likely move more freely than other chromatin

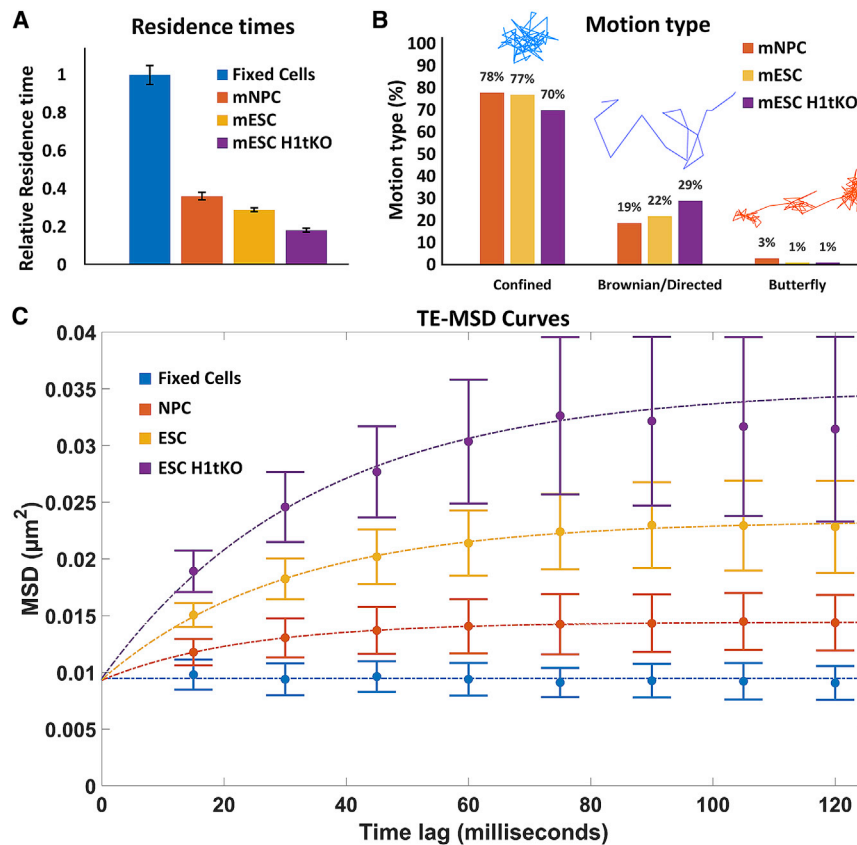


Figure 3. H2B Has a Shorter Residence Time and Moves More Dynamically within Chromatin in mESCs Compared to mNPCs

(A) Normalized residence times measured using slow SPT (500-ms exposure time) in fixed cells (cyan), mNPCs (orange), mESCs (yellow), and mESC-H1tKO (mESCs in which three isoforms of H1 has been knocked out) (purple). Values were obtained from the double exponential decay function fitting of the survival fraction distribution of the trajectories over time and normalized to the value obtained in fixed cells. The bar corresponds to the mean and the error bars correspond to the 95% confidence interval values that are obtained from fitting the data to the model. $n = 245, 3,200, 2,593,$ and 887 trajectories were used for the analysis for fixed cells, mNPCs, mESCs, and mESC-H1tKO, respectively.

(B) Proportion of trajectories showing confined, Brownian/directed or a mixture of confined and Brownian/directed (butterfly) motion. $n = 4,021, 5,295,$ and $2,436$ trajectories for mNPCs, mESCs, and mESC-H1tKO were used, respectively.

(C) Mean square displacement (MSD) versus time plot for the different cell types. The ensemble MSD average of all the displacements for each time lag and the standard deviation are displayed. A circle confined diffusion model was used to fit the time-ensemble MSD (TE-MSD) (dashed lines), and the average diffusion coefficient and radius of confinement were obtained for each cell type. For fixed cells, all the tracks were used without filtering ($n = 284$ trajectories). For the rest, only the confined trajectories were used ($n = 543, 860,$ and 370 trajectories for mNPCs, mESCs, and mESC-H1tKO, respectively).

domains embedded within chromosomes. In mouse, their length varies between 50 and 150 kbp (Starling et al., 1990) (or 100–750 nucleosomes) and their volume correlates with their length (Bandaria et al., 2016; Neguembor et al., 2018). These measurements showed that at these short timescales (i.e., tens of milliseconds), telomere and centromere mobility was much smaller than H2B and comparable to the mobility measured in fixed cells (Figures 4B and 4C). While the mobility of telomeric H2B (i.e., H2B overlapping with telomeres) was slightly lower than non-telomeric H2B, even telomeric H2B mobility was substantially higher than the mobility of large telomeric regions (Figure S5D). At longer timescales (i.e., tens of seconds), telomeres and centromeres showed dynamic behavior, exploring areas ranging from $0.5 \times 0.5 \mu\text{m}^2$ to $1.5 \times 1.5 \mu\text{m}^2$, consistent with previous studies (Neguembor et al., 2018; Verdaasdonk et al., 2013). Hence, large chromatin domains are relatively immobile at short timescales compared to H2B and the latter likely corresponds to the mobility of individual nucleosomes themselves or small groups of nucleosomes within the chromatin fiber, showing that nucleosomes can move within chromatin domains in a manner independent of the domain itself. We note that our use of fast exposure times (10 ms) and bright, photostable fluorophores drastically improved the sensitivity of our H2B mobility measurement, enabling us to detect such fine nucleosome movements.

Dynamics of Both Heterochromatic and Euchromatic H2B Are Affected by the Process of Differentiation

Overlaying the H2B motion trajectories on Hoechst images of DNA allowed us to further explore the differences in the local H2B dynamics between heterochromatic and euchromatic regions of the different cell types (Figure 5A). We subcategorized the H2B trajectories based on their overlap with high- or low-intensity regions in the Hoechst images, corresponding to more heterochromatic or more euchromatic regions, respectively (Figure 5A). This analysis showed that H2B in heterochromatic regions was more confined than that in euchromatic regions in all three cell types (Figure 5B). The more confined mobility of heterochromatic H2B was further confirmed by tracking H2B that overlapped with telomeres. H2B tracks overlapping with telomeres showed on average more confined mobility than trajectories that did not overlap with telomeres (Figure S5D). Interestingly, there were significant differences between the radius of confinement of both heterochromatic and euchromatic H2B among the three cell types; euchromatic H2B in mESCs-H1tKO was the least confined, and the heterochromatic H2B in mNPCs were the most confined (Figure 5B). Hence, our results demonstrate that the mobility of both the heterochromatic and euchromatic H2B is affected by differentiation (Figure 5B).

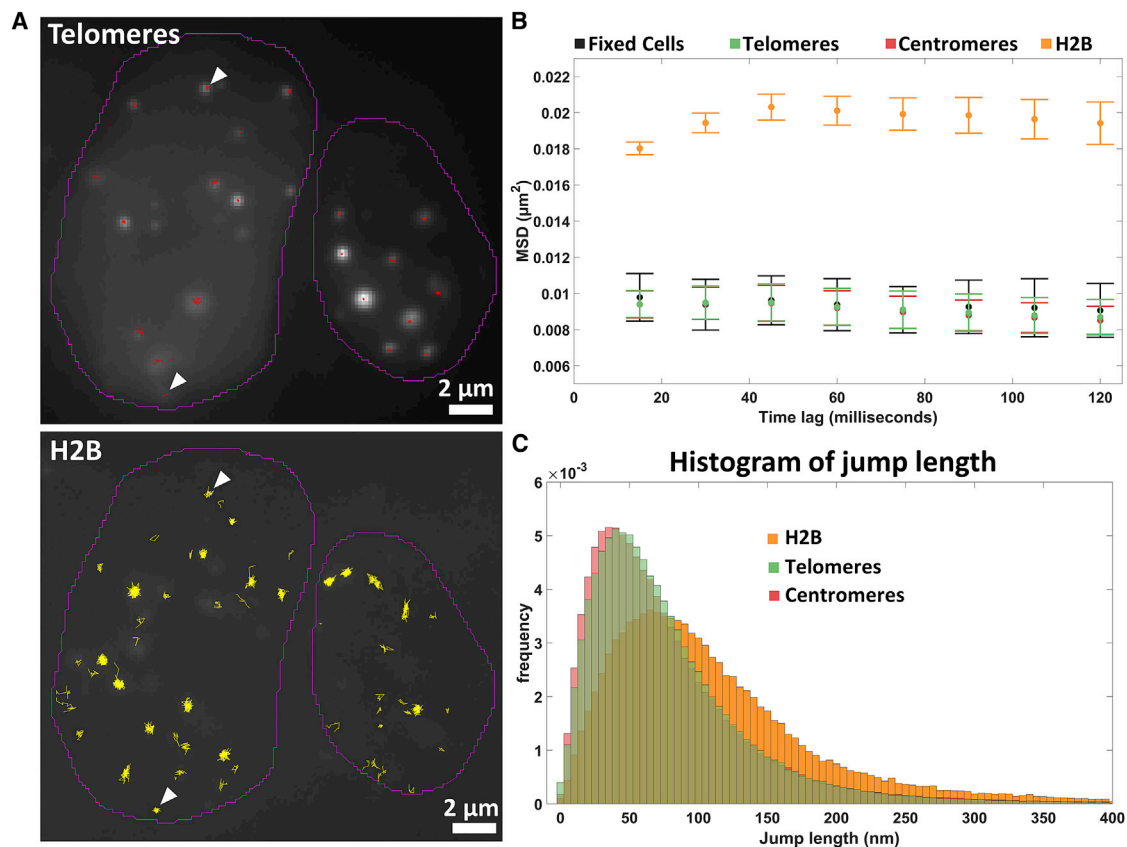


Figure 4. Telomere Motion Takes Place at Much Slower Timescales Compared to H2B Motion

(A) Upper panel shows telomere trajectories (red) overlapped on a maximal projection image of telomeres. The tracks were cropped so that their track length is in the same scale as for H2B trajectories for visualization purposes. Lower panel shows the corresponding H2B trajectories from the two-color SMT experiment. White arrows indicate example trajectories where telomeres and nucleosomes overlap. A maximum spatial threshold of 250 nm between the telomere trajectory and the H2B trajectory position was imposed in order to assign a nucleosome trajectory to a telomeric region.

(B) TE-MSD curves comparing H2B in live cells to telomeres, centromeres and H2B in fixed cells. The mean and the standard deviation of the MSD of all the trajectories for each time lag is plotted. Telomere and centromere MSD curves overlap with MSD curve of H2B in fixed cells, whereas H2B in live cells is more dynamic. $n = 284, 9,135, 10,660,$ and $11,752$ trajectories were used for fixed cells, telomeres, centromeres, and H2B, respectively.

(C) Histogram of frame-to-frame jump distribution for telomeres (orange), centromeres (green), and H2B in live cells (cyan). $n = 11,752, 9,135,$ and $10,660$ trajectories were analyzed for H2B, telomeres, and centromeres, respectively.

DISCUSSION

Recent high-resolution imaging experiments, including super-resolution fluorescence microscopy and electron tomography, have revealed a complex picture of chromatin structure in which chromatin is composed of 10-nm fibers that form nucleosome clusters (or clutches) of different levels of nucleosome density (Fussner et al., 2012; Otterstrom et al., 2019; Ricci et al., 2015). The level of chromatin fiber compaction as well as the nucleosome kinetics likely influence the activation or repression of key lineage and pluripotency genes during development. For this reason, it is paramount to study these chromatin fiber features in somatic and stem cells. Here, we show that chromatin structure and kinetics can be directly measured and interpreted using complementary techniques, including mesoscale modeling, super-resolution imaging, and SMT. Specifically, using mesoscale, coarse-grained modeling of large nucleosome assemblies incorporating realistic nucleosome positions based

on MNase-seq data with experimentally measured linker histone and acetylation densities, we showed that the nucleosome clutch differences of a model pluripotency gene (*Pou5f1*) correlate with the global state of clutch conformation seen in mESCs and mNPCs by super-resolution experiments. Furthermore, the enhanced chromatin compaction during differentiation is directly related to changes in nucleosome positioning, amount of linker histones, and acetylation patterns. In a separate study (Portillo-Ledesma et al., 2020b), we varied these physical parameters independently in the fiber composition within the mesoscale model to generate experimentally testable hypotheses about the most important mechanisms responsible for nucleosome clutch formation and reorganization in differentiation. Overall, we find that nucleosome positions profoundly affect clutch patterns. In particular, the placement and length of NFRs along with linker lengths dictate clutch size and separations. Specifically, higher linker histone densities generally produce larger/compact clutches by a chromatin compaction mechanism, while higher

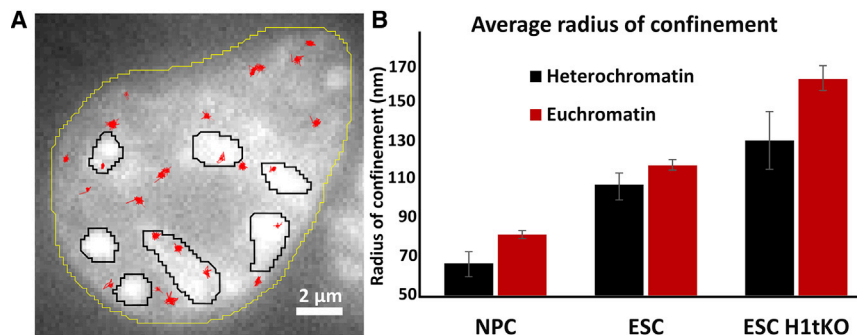


Figure 5. Mobility of Both Euchromatic and Heterochromatic H2B Changes upon Cell Differentiation

(A) Image of a mESC labeled with Hoechst 33342 showing the cell nucleus (yellow region of interest [ROI]). Euchromatin (low-intensity) and heterochromatin (high-intensity [black ROIs]) regions and the corresponding H2B trajectories within each region (red) are shown.

(B) Bar plot showing the radius of confinement estimation from a circle confined diffusion model for H2B moving within euchromatic (red) and heterochromatic (black) regions in the different cell types. Mean and 95% confidence intervals are plotted. Only confined trajectories were used ($n = 543, 860, \text{ and } 370$ trajectories for mNPCs, mESCs, and mESC-H1tKO, respectively).

acetylation levels produce smaller/loose clutches by a structure-dependent mechanism of chromatin unfolding. Chromatin fibers corresponding to genes are heterogeneous in terms of these parameters, containing variable linker lengths, NFRs, various acetylation islands, and linker histone (LH) binding regions and hence comprise a complex combination of these global and local folding patterns observed in synthetic fibers (Portillo-Ledesma and Schlick, 2020a).

In the current study, we observed that the model further revealed that the changes to clutch size upon differentiation are likely due to increased hairpin and hierarchical looping. These hierarchical looping motifs were previously proposed based on comparison of modeled fibers with internucleosome contact probability profiles obtained by electron microscopy imaging of cross-linked metaphase chromosomes (Grigoryev et al., 2016). While experimental data on local chromatin folding in cells at nucleosome resolution are very limited, recent micro-C contact maps of mammalian cells are compatible with the presence of extended two-start zigzag fibers (Hsieh et al., 2020; Krietenstein et al., 2020), consistent with the proposed hierarchical looping model. Moreover, in micro-C contact maps, small clutches of $\sim 3\text{--}10$ nucleosomes were observed to be organized in the zigzag helical orientation and formed stacks of short tri- or tetra-nucleosome zigzag motifs (Krietenstein et al., 2020). These results are in full agreement with our previous super-resolution data (Ricci et al., 2015) and current modeling results on clutch organization showing an average of 6–18 nucleosomes per clutch in mammalian cells with nucleosomes inside clutches organized in a zigzag configuration. The increased hierarchical looping in NPCs ultimately might contribute to the silencing of *Pou5f1* gene. We found that the expression level of *Pou5f1* decreased by 7-fold upon differentiation of mESCs into mNPCs, whereas the clutch size and compaction in the mesoscale model increased by 3-fold and 2-fold, respectively. In the future, it would be interesting to determine if the fold-change in expression quantitatively relates to the changes in clutch configuration of multiple genes, which would suggest that clutches exclude transcriptional machinery in direct relation to their size and compaction.

While an ideal model would contain the specific location for nucleosome positions, linker histones, histone acetylation, other epigenetic modifications, and even binding of proteins, it is diffi-

cult to obtain all these parameters from one or multiple set of experiments carried out in the same experimental conditions. Using average values for these parameters has in the past proven valid and valuable on the *GATA-4* (Bascom et al., 2016) and *HOXC* (Bascom et al., 2019) genes and on epigenetically marked chromatin (Rao et al., 2017). Averaging is also a feature of many methods used to study chromatin architecture, including chromosome conformation capture methods, which provide invaluable insight into the 3D genome folding despite averaging over millions of cells. Our model was able to further reproduce experimental data of single cells obtained using super-resolution microscopy and hence can integrate and reconcile single cell and bulk data of chromatin structure. In the future, refining the model by including parameters relative to additional epigenetic marks and protein binding data obtained using chromatin immunoprecipitation sequencing (ChIP-seq) analysis in different cell types should provide more precise configuration of clutch patterns of various genes in different cell types.

While our mesoscale nucleosome-resolution model is DNA sequence independent, it offers a valuable approach to study chromatin fibers extending to small gene sizes as a function of key parameters like linker lengths, H1 binding levels, and histone acetylation marks. Previous *in vitro* experimental work has shown sequence dependence of nucleosome occupancy (Chung and Vingron, 2009; Struhl and Segal, 2013), although most recent studies showed that DNA independent factors are more important and account for a role of the transcriptional state of the region as key determinant of nucleosome occupancy (Chereji et al., 2018). Importantly, in our study, we model the same chromatin region of the *Pou5f1* locus in ESCs and NPCs, which excludes that sequence dependence affects clutch assembly and nucleosome positioning at least in this specific locus.

SMT has been a powerful tool for studying the nuclear target search and binding mechanisms of dynamic proteins like transcription factors (Chen et al., 2014; Hansen et al., 2020; Izeddin et al., 2014; Liu et al., 2014; Normanno et al., 2015; Prabhat et al., 2004). Only few other studies applied SMT to measure histone dynamics within the nucleus (Lerner et al., 2020; Nagashima et al., 2019; Nozaki et al., 2017). In one case, the use of dim fluorescent proteins that are prone to photobleaching mostly limited the analysis to large chromatin domains (100–200 nm) rather

than individual histones (Nozaki et al., 2017). In a second study, Halo tagging was used to study how histone dynamics are impacted in transcriptionally perturbed retinal pigmented epithelial (RPE) cells, but the mechanisms that constrain histone mobility under basal conditions and how these dynamics change in different cell types were not explored (Nagashima et al., 2019). More recently, using fast-SMT of Halo-tagged H2B, it was shown that histones have a complex mobility landscape within the nucleus of hepatic cells and that different transcription factors interact with distinct chromatin mobility ranges (Lerner et al., 2020). Overall, it is emerging that histone and chromatin mobility is functionally significant, underscoring the importance of further studies to dissect this mobility and underlying mechanisms that restrain histone dynamics in different cell types, as we did here. Using slow and fast SMT in several cell types, we show quantitatively at the single-histone level that there are changes in H2B residence times and local H2B motion in mESCs, mESCs-H1tKO, and mNPCs consistent with the measured structural changes. H2B mobility was more constrained within heterochromatic regions composed of large, compacted nucleosome clutches compared to euchromatic regions. The residence time and local mobility of both hetero- and euchromatic H2B also depended on cell type as H2B in differentiated cells containing larger and more compacted nucleosome clutches were more stable than H2B in mESCs. Importantly, the measured dynamics likely correspond to movement of individual H2Bs within their local chromatin fiber, as larger genomic regions like telomeres and centromeres were immobile at these timescales. The measured H2B dynamics may correspond to nucleosome sliding as well as other types of nucleosome destabilization within chromatin. Interestingly, the local, confined motion of H2B and its residence time within the chromatin fiber was significantly affected by knockout of the linker histone H1. The mESCs-H1tKO also had the smallest nucleosome clutches, as measured using super-resolution microscopy (Ricci et al., 2015). Hence, presence of a large number of tightly compacted nucleosomes within clutches, which are likely stabilized by the linker histone, can potentially constrain H2B motion and stabilize nucleosomes. Previous FRAP studies found no difference in H1 dynamics, a relatively mobile protein, between WT and H1-knockout cells (Melcer et al., 2012), highlighting the importance of using a sensitive method such as SMT to elucidate the differences in the dynamics of a less mobile protein like H2B and the impact of linker histones on chromatin protein dynamics. It will be interesting to further probe the molecular mechanisms responsible for nucleosome stability and local motion using SMT and knockout models. Measuring the impact of these dynamics on transcription factor binding to chromatin and gene activation will further help unravel the relation between genome organization and function. Finally, our mesoscale model sets up a framework to apply Brownian dynamics to study dynamic processes and folding pathways, which in the future will provide valuable comparison to experimental SMT data.

STAR★METHODS

Detailed methods are provided in the online version of this paper and include the following:

- **KEY RESOURCES TABLE**
- **RESOURCE AVAILABILITY**
 - Lead Contact
 - Materials Availability
 - Data and Code Availability
- **EXPERIMENTAL MODEL AND SUBJECT DETAILS**
 - Cell culture conditions and generation of cell lines
- **METHOD DETAILS**
 - Cell Labeling for Single Molecule Tracking Imaging
 - Imaging
 - 2-Color Imaging
 - Tracking
 - Trajectory Analysis
 - Trajectory Classification
 - Diffusion Coefficients
 - Circle Confined Diffusion Model
 - Residence Times
 - Mesoscale Modeling of mESC and mNPC Chromatin Fibers
 - Chromatin Structure Analysis of Coarse-Grained Model
 - Gene Expression Analysis
 - Protein Extraction and Western Blot
 - Contact Probability Matrices
 - Zigzag Geometry Inside the Clutches
 - SMLM Image Generation
 - Cluster Analysis
- **QUANTIFICATION AND STATISTICAL ANALYSIS**

SUPPLEMENTAL INFORMATION

Supplemental Information can be found online at <https://doi.org/10.1016/j.celrep.2020.108614>.

ACKNOWLEDGMENTS

This work was supported by a University of Pennsylvania Epigenetics Pilot Award (M.L.); an NSF Center for Engineering and Mechanobiology (CEMB) Pilot Award (M.L.); a Linda Pechenik Montague Investigator Award (M.L.); the European Union's Horizon 2020 Research and Innovation Programme (Cell-Viewer grant 686637 to M.L., M.P.C., and E.M.); Ministerio de Ciencia, Innovación y Universidades (BFU2017-86760-P [AEI/FEDER, UE]) and Secretaria d'Universitats i Recerca del Departament d'Empresa i Coneixement de la Generalitat de Catalunya (AGAUR grant 2017 SGR 689 to M.P.C.); National NSFC grant 319711771003712 (M.P.C.); National Institutes of Health, National Institute of General Medical Sciences awards R01-GM055264 and R35-GM122562; Phillip-Morris USA and Phillip-Morris International (T.S.); People Program (Marie Curie Actions) FP7/2007–2013 under REA grant 608959 (M.V.N.); and Juan de la Cierva-Incorporación 2017 (M.V.N.).

AUTHOR CONTRIBUTIONS

Conceptualization, M.L. and M.P.C.; Methodology, P.A.G.-G., S.P.-L., T.S., and M.L.; Modeling, S.P.L. and T.S.; Software, P.A.G.-G., S.P.-L.; Experiments, P.A.G.-G., M.V.N., M.P., W.O., and T.R.; Reagents, cell lines and other resources: M.V.N., M.P., W.O., T.R., E.M., and S.W.; Analysis, P.A.G.-G. and S.P.-L.; Writing – Original Draft: M.L., M.P.C., P.A.G.-G., and T.S.; Supervision, M.L., M.P.C., and T.S.; Funding Acquisition, M.L., M.P.C., T.S., and E.M. All authors read and provided comments on the manuscript.

DECLARATION OF INTERESTS

The authors declare no competing interests.

Received: February 28, 2020

Revised: October 29, 2020

Accepted: December 16, 2020

Published: January 12, 2021

REFERENCES

Arya, G., and Schlick, T. (2006). Role of histone tails in chromatin folding revealed by a mesoscopic oligonucleosome model. *Proc. Natl. Acad. Sci. USA* *103*, 16236–16241.

Arya, G., and Schlick, T. (2009). A tale of tails: how histone tails mediate chromatin compaction in different salt and linker histone environments. *J. Phys. Chem. A* *113*, 4045–4059.

Arya, G., Zhang, Q., and Schlick, T. (2006). Flexible histone tails in a new mesoscopic oligonucleosome model. *Biophys. J.* *91*, 133–150.

Aulicino, F., Theka, I., Ombrato, L., Lluís, F., and Cosma, M.P. (2014). Temporal perturbation of the Wnt signaling pathway in the control of cell reprogramming is modulated by TCF1. *Stem Cell Reports* *2*, 707–720.

Ball, D.A., Mehta, G.D., Salomon-Kent, R., Mazza, D., Morisaki, T., Mueller, F., McNally, J.G., and Karpova, T.S. (2016). Single molecule tracking of Ace1p in *Saccharomyces cerevisiae* defines a characteristic residence time for non-specific interactions of transcription factors with chromatin. *Nucleic Acids Res.* *44*, e160.

Bandaria, J.N., Qin, P., Berk, V., Chu, S., and Yildiz, A. (2016). Shelterin protects chromosome ends by compacting telomeric chromatin. *Cell* *164*, 735–746.

Bascom, D.G., and Schlick, T. (2018). Mesoscale modeling of chromatin fibers. In *Nuclear Architecture and Dynamics*, C. Lavelle and J.-M. Victor, eds. (Elsevier), pp. 123–147.

Bascom, G.D., Sanbonmatsu, K.Y., and Schlick, T. (2016). Mesoscale modeling reveals hierarchical looping of chromatin fibers near gene regulatory elements. *J. Phys. Chem. B* *120*, 8642–8653.

Bascom, G.D., Myers, C.G., and Schlick, T. (2019). Mesoscale modeling reveals formation of an epigenetically driven HOXC gene hub. *Proc. Natl. Acad. Sci. USA* *116*, 4955–4962.

Beringer, M., Pisano, P., Di Carlo, V., Blanco, E., Chammas, P., Vizán, P., Gutiérrez, A., Aranda, S., Payer, B., Wierer, M., and Di Croce, L. (2016). EPOF functionally links Elongin and Polycomb in pluripotent stem cells. *Mol. Cell* *64*, 645–658.

Boettiger, A.N., Bintu, B., Moffitt, J.R., Wang, S., Beliveau, B.J., Fudenberg, G., Imakaev, M., Mirny, L.A., Wu, C.T., and Zhuang, X. (2016). Super-resolution imaging reveals distinct chromatin folding for different epigenetic states. *Nature* *529*, 418–422.

Bryan, L.C., Weilandt, D.R., Bachmann, A.L., Kilic, S., Lechner, C.C., Odermatt, P.D., Fantner, G.E., Georgeon, S., Hantschel, O., Hatzimanikatis, V., and Fierz, B. (2017). Single-molecule kinetic analysis of HP1-chromatin binding reveals a dynamic network of histone modification and DNA interactions. *Nucleic Acids Res.* *45*, 10504–10517.

Butler, P.J.G., and Thomas, J.O. (1998). Dinucleosomes show compaction by ionic strength, consistent with bending of linker DNA. *J. Mol. Biol.* *287*, 401–407.

Chen, K., Xi, Y., Pan, X., Li, Z., Kaestner, K., Tyler, J., Dent, S., He, X., and Li, W. (2013). DANPOS: dynamic analysis of nucleosome position and occupancy by sequencing. *Genome Res.* *23*, 341–351.

Chen, J., Zhang, Z., Li, L., Chen, B.C., Revyakin, A., Hajj, B., Legant, W., Dahan, M., Lionnet, T., Betzig, E., et al. (2014). Single-molecule dynamics of enhancosome assembly in embryonic stem cells. *Cell* *156*, 1274–1285.

Chen, H., Levo, M., Barinov, L., Fujioaka, M., Jaynes, J.B., and Gregor, T. (2018). Dynamic interplay between enhancer-promoter topology and gene activity. *Nat. Genet.* *50*, 1296–1303.

Chereji, R.V., Ramachandran, S., Bryson, T.D., and Henikoff, S. (2018). Precise genome-wide mapping of single nucleosomes and linkers in vivo. *Genome Biol.* *19*, 19.

Chuang, C.-H., Carpenter, A.E., Fuchsova, B., Johnson, T., de Lanerolle, P., and Belmont, A.S. (2006). Long-range directional movement of an interphase chromosome site. *Curr. Biol.* *16*, 825–831.

Chung, H.-R., and Vingron, M. (2009). Sequence-dependent nucleosome positioning. *J. Mol. Biol.* *386*, 1411–1422.

Collepardo-Guevara, R., and Schlick, T. (2014). Chromatin fiber polymorphism triggered by variations of DNA linker lengths. *Proc. Natl. Acad. Sci. USA* *111*, 8061–8066.

Collepardo-Guevara, R., Portella, G., Vendruscolo, M., Frenkel, D., Schlick, T., and Orozco, M. (2015). Chromatin unfolding by epigenetic modifications explained by dramatic impairment of internucleosome interactions: a multiscale computational study. *J. Am. Chem. Soc.* *137*, 10205–10215.

Davey, C.A., Sargent, D.F., Luger, K., Maeder, A.W., and Richmond, T.J. (2002). Solvent mediated interactions in the structure of the nucleosome core particle at 1.9 Å resolution. *J. Mol. Biol.* *319*, 1097–1113.

Drew, H.R., and Travers, A.A. (1985). DNA bending and its relation to nucleosome positioning. *J. Mol. Biol.* *186*, 773–790.

Ester, M., Kriegl, H.-P., Sander, J., and Xu, X. (1996). A density-based algorithm for discovering clusters in large spatial databases with noise. In *Proceedings of the 2nd International Conference on Knowledge Discovery and Data Mining (AAAI Press)*.

Fan, Y., Nikitina, T., Morin-Kensicki, E.M., Zhao, J., Magnuson, T.R., Woodcock, C.L., and Skoultschi, A.I. (2003). H1 linker histones are essential for mouse development and affect nucleosome spacing in vivo. *Mol. Cell. Biol.* *23*, 4559–4572.

Fan, Y., Nikitina, T., Zhao, J., Fleury, T.J., Bhattacharyya, R., Bouhassira, E.E., Stein, A., Woodcock, C.L., Skoultschi, A.I., Morin-kensicki, E.M., et al. (2005). Histone H1 depletion in mammals alters global chromatin structure but causes specific changes in gene regulation. *Cell* *123*, 1199–1212.

Fussner, E., Strauss, M., Djuric, U., Li, R., Ahmed, K., Hart, M., Ellis, J., and Bazett-Jones, D.P. (2012). Open and closed domains in the mouse genome are configured as 10-nm chromatin fibres. *EMBO Rep.* *13*, 992–996.

Garcia-Ramirez, M., Dong, F., and Ausio, J. (1992). Role of the histone “tails” in the folding of oligonucleosomes depleted of histone H1. *J. Biol. Chem.* *267*, 19587–19595.

Grigoryev, S.A., Bascom, G., Buckwalter, J.M., Schubert, M.B., Woodcock, C.L., and Schlick, T. (2016). Hierarchical looping of zigzag nucleosome chains in metaphase chromosomes. *Proc. Natl. Acad. Sci. USA* *113*, 1238–1243.

Grimm, J.B., English, B.P., Chen, J., Slaughter, J.P., Zhang, Z., Revyakin, A., Patel, R., Macklin, J.J., Normanno, D., Singer, R.H., et al. (2015). A general method to improve fluorophores for live-cell and single-molecule microscopy. *Nat Methods* *12*, 244–250.

Hansen, A.S., Pustova, I., Cattoglio, C., Tjian, R., and Darzacq, X. (2017). CTCF and cohesin regulate chromatin loop stability with distinct dynamics. *eLife* *6*, 1–33.

Hansen, A.S., Amitai, A., Cattoglio, C., Tjian, R., and Darzacq, X. (2020). Guided nuclear exploration increases CTCF target search efficiency. *Nat. Chem. Biol.* *16*, 257–266.

Higashi, T., Matsunaga, S., Isobe, K., Morimoto, A., Shimada, T., Kataoka, S., Watanabe, W., Uchiyama, S., Itoh, K., and Fukui, K. (2007). Histone H2A mobility is regulated by its tails and acetylation of core histone tails. *Biochem. Biophys. Res. Commun.* *357*, 627–632.

Hsieh, T.S., Cattoglio, C., Slobodyanyuk, E., Hansen, A.S., Rando, O.J., Tjian, R., and Darzacq, X. (2020). Resolving the 3D landscape of transcription-linked mammalian chromatin folding. *Mol. Cell* *78*, 539–553.e8.

Izeddin, I., Récamier, V., Bosanac, L., Cissé, I.I., Boudarene, L., Dugast-Darzacq, C., Proux, F., Bénichou, O., Voituriez, R., Bensaude, O., et al. (2014). Single-molecule tracking in live cells reveals distinct target-search strategies of transcription factors in the nucleus. *eLife* *3*, 1–27.

- Jian, H., Vologodskii, A.V., and Schlick, T. (1997). A combined wormlike-chain and bead model for dynamic simulations of long linear DNA. *J. Comp. Physiol.* *136*, 168–179.
- Kimura, H. (2005). Histone dynamics in living cells revealed by photobleaching. *DNA Repair (Amst.)* *4*, 939–950.
- Kimura, H., and Cook, P.R. (2001). Kinetics of core histones in living human cells: little exchange of H3 and H4 and some rapid exchange of H2B. *J. Cell Biol.* *153*, 1341–1353.
- Konermann, S., Brigham, M.D., Trevino, A.E., Jung, J., Abudayyeh, O.O., Barcena, C., Hsu, P.D., Habib, N., Gootenberg, J.S., Nishimasu, H., et al. (2015). Genome-scale transcriptional activation by an engineered CRISPR-Cas9 complex. *Nature* *517*, 583–588.
- Krietenstein, N., Abraham, S., Venev, S.V., Abdennur, N., Gibcus, J., Hsieh, T.S., Parsi, K.M., Yang, L., Maehr, R., Mirny, L.A., et al. (2020). Ultrastructural details of mammalian chromosome architecture. *Mol. Cell* *78*, 554–565.e7.
- Lakadamyali, M., and Cosma, M.P. (2020). Visualizing the genome in high resolution challenges our textbook understanding. *Nat. Methods* *17*, 371–379.
- Lerner, J., Gomez-Garcia, P.A., McCarthy, R.L., Liu, Z., Lakadamyali, M., and Zaret, K.S. (2020). Two-parameter mobility assessments discriminate diverse regulatory factor behaviors in chromatin. *Mol. Cell* *79*, 677–688.e6.
- Levitt, M., and Warshel, A. (1975). Computer simulation of protein folding. *Nature* *253*, 694–698.
- Liu, Z., Legant, W.R., Chen, B.C., Li, L., Grimm, J.B., Lavis, L.D., Betzig, E., and Tjian, R. (2014). 3D imaging of Sox2 enhancer clusters in embryonic stem cells. *eLife* *3*, e04236.
- Luque, A., Collepardo-Guevara, R., Grigoryev, S., and Schlick, T. (2014). Dynamic condensation of linker histone C-terminal domain regulates chromatin structure. *Nucleic Acids Res.* *42*, 7553–7560.
- Manzo, C., and Garcia-Parajo, M.F. (2015). A review of progress in single particle tracking: from methods to biophysical insights. *Rep. Prog. Phys.* *78*, 124601.
- Manzo, C., Torreno-Pina, J.A., Massignan, P., Lapeyre, G.J., Lewenstein, M., and Garcia Parajo, M.F. (2015). Weak ergodicity breaking of receptor motion in living cells stemming from random diffusivity. *Phys. Rev. X* *5*, 011021.
- Mazza, D., Abernathy, A., Golob, N., Morisaki, T., and McNally, J.G. (2012). A benchmark for chromatin binding measurements in live cells. *Nucleic Acids Res.* *40*, e119.
- Melcer, S., Hezroni, H., Rand, E., Nissim-Rafinia, M., Skoultchi, A., Stewart, C.L., Bustin, M., and Meshorer, E. (2012). Histone modifications and lamin A regulate chromatin protein dynamics in early embryonic stem cell differentiation. *Nat. Commun.* *3*, 910.
- Meshorer, E., Yellajoshula, D., George, E., Scambler, P.J., Brown, D.T., and Misteli, T. (2006). Hyperdynamic plasticity of chromatin proteins in pluripotent embryonic stem cells. *Dev. Cell* *10*, 105–116.
- Metropolis, N., and Ulam, S. (1949). The Monte Carlo method. *J. Am. Stat. Assoc.* *44*, 335–341.
- Michalet, X. (2010). Mean square displacement analysis of single-particle trajectories with localization error: Brownian motion in an isotropic medium. *Phys. Rev. E Stat. Nonlin. Soft Matter Phys.* *82*, 041914.
- Michalet, X., and Berglund, A.J. (2012). Optimal diffusion coefficient estimation in single-particle tracking. *Phys. Rev. E Stat. Nonlin. Soft Matter Phys.* *85*, 061916.
- Mieczkowski, J., Cook, A., Bowman, S.K., Mueller, B., Alver, B.H., Kundu, S., Deaton, A.M., Urban, J.A., Larschan, E., Park, P.J., et al. (2016). MNase titration reveals differences between nucleosome occupancy and chromatin accessibility. *Nat. Commun.* *7*, 11485.
- Monnier, N., Barry, Z., Park, H.Y., Su, K.-C., Katz, Z., English, B.P., Dey, A., Pan, K., Cheeseman, I.M., Singer, R.H., and Bathe, M. (2015). Inferring transient particle transport dynamics in live cells. *Nat. Methods* *12*, 838–840.
- Nagashima, R., Hibino, K., Ashwin, S.S., Babokhov, M., Fujishiro, S., Imai, R., Nozaki, T., Tamura, S., Tani, T., Kimura, H., et al. (2019). Single nucleosome imaging reveals loose genome chromatin networks via active RNA polymerase II. *J. Cell Biol.* *218*, 1511–1530.
- Nandi, A., Heinrich, D., and Lindner, B. (2012). Distributions of diffusion measures from a local mean-square displacement analysis. *Phys. Rev. E Stat. Nonlin. Soft Matter Phys.* *86*, 021926.
- Neguembor, M.V., Sebastian-Perez, R., Aulicino, F., Gomez-Garcia, P.A., Cosma, M.P., and Lakadamyali, M. (2018). (Po)STAC (Polycistronic SunTAg modified CRISPR) enables live-cell and fixed-cell super-resolution imaging of multiple genes. *Nucleic Acids Res.* *46*, e30.
- Neumann, F.R., Dion, V., Gehlen, L.R., Tsai-Pflugfelder, M., Schmid, R., Taddei, A., and Gasser, S.M. (2012). Targeted INO80 enhances subnuclear chromatin movement and ectopic homologous recombination. *Genes Dev.* *26*, 369–383.
- Normanno, D., Boudarène, L., Dugast-Darzacq, C., Chen, J., Richter, C., Proux, F., Bénichou, O., Voituriez, R., Darzacq, X., and Dahan, M. (2015). Probing the target search of DNA-binding proteins in mammalian cells using TetR as model searcher. *Nat. Commun.* *6*, 7357.
- Nozaki, T., Imai, R., Tanbo, M., Nagashima, R., Tamura, S., Tani, T., Joti, Y., Tomita, M., Hibino, K., Kanemaki, M.T., et al. (2017). Dynamic organization of chromatin domains revealed by super-resolution live-cell imaging. *Mol. Cell* *67*, 282–293.e7.
- Nozaki, T., Hudson, D.F., Tamura, S., and Maeshima, K. (2018). Dynamic chromatin folding in the cell. In *Nuclear Architecture and Dynamics*, C. Lavelle and J.-M. Victor, eds. (Elsevier), pp. 101–122.
- Otterstrom, J., Castells-Garcia, A., Vicario, C., Gomez-Garcia, P.A., Cosma, M.P., and Lakadamyali, M. (2019). Super-resolution microscopy reveals how histone tail acetylation affects DNA compaction within nucleosomes in vivo. *Nucleic Acids Res.* *47*, 8470–8484.
- Ou, H.D., Phan, S., Deerinck, T.J., Thor, A., Ellisman, M.H., and O’Shea, C.C. (2017). ChromEMT: visualizing 3D chromatin structure and compaction in interphase and mitotic cells. *Science* *357*, eaag0025.
- Perišić, O., Collepardo-Guevara, R., and Schlick, T. (2010). Modeling studies of chromatin fiber structure as a function of DNA linker length. *J. Mol. Biol.* *403*, 777–802.
- Portillo-Ledesma, S., and Schlick, T. (2020a). Bridging chromatin structure and function over a range of experimental spatial and temporal scales by molecular modeling. *Wiley Interdiscip. Rev. Comput. Mol. Sci.* *10*, 1–20.
- Portillo-Ledesma, S., Tsao, L.H., Wagley, M., Lakadamyali, M., Pia Cosma, M., and Schlick, T. (2020b). Nucleosome Clutches are Regulated by Chromatin Internal Parameters. *Journal of Molecular Biology*, Published online November 9, 2020. <https://doi.org/10.1016/j.jmb.2020.11.001>.
- Prabhat, P., Ram, S., Ward, E.S., and Ober, R.J. (2004). Simultaneous imaging of different focal planes in fluorescence microscopy for the study of cellular dynamics in three dimensions. *IEEE Trans. Nanobioscience* *3*, 237–242.
- Rao, S.S.P., Huang, S.-C., Glenn St Hilaire, B., Engreitz, J.M., Perez, E.M., Kieffer-Kwon, K.-R., Sanborn, A.L., Johnstone, S.E., Bascom, G.D., Bochkov, I.D., et al. (2017). Cohesin loss eliminates all loop domains. *Cell* *171*, 305–320.e24.
- Rhodes, J.D.P., Haarhuis, J.H.I., Grimm, J.B., Rowland, B.D., Lavis, L.D., and Nasmyth, K.A. (2017). Cohesin can remain associated with chromosomes during DNA replication. *Cell Rep.* *20*, 2749–2755.
- Ricci, M.A., Manzo, C., Garcia-Parajo, M.F., Lakadamyali, M., and Cosma, M.P. (2015). Chromatin fibers are formed by heterogeneous groups of nucleosomes in vivo. *Cell* *160*, 1145–1158.
- Roh, T.Y., Wei, G., Farrell, C.M., and Zhao, K. (2007). Genome-wide prediction of conserved and nonconserved enhancers by histone acetylation patterns. *Genome Res.* *17*, 74–81.
- Rosenbluth, M.N., and Rosenbluth, A.W. (1955). Monte Carlo calculation of the average extension of molecular chains. *J. Chem. Phys.* *23*, 356–359.
- Sander, J., Ester, M., Kriegel, H.P., and Xu, X. (1998). Density-based clustering in spatial databases: The algorithm GDBSCAN and its applications. *Data Min. Knowl. Discov.* *2*, 169–194.

- Schindelin, J., Arganda-Carreras, I., Frise, E., Kaynig, V., Longair, M., Pietzsch, T., Preibisch, S., Rueden, C., Saalfeld, S., Schmid, B., et al. (2012). Fiji: an open-source platform for biological-image analysis. *Nat. Methods* **9**, 676–682.
- Schlesinger, S., and Meshorer, E. (2019). Open chromatin, epigenetic plasticity, and nuclear organization in pluripotency. *Dev. Cell* **48**, 135–150.
- Shaban, H., Barth, R., Recoules, L., and Bystricky, K. (2018). Hi-D: nanoscale mapping of nuclear dynamics in single living cells. *BioRxiv*.
- Shen, H., Tauzin, L.J., Baiyasi, R., Wang, W., Moringo, N., Shuang, B., and Landes, C.F. (2017). Single particle tracking: from theory to biophysical applications. *Chem. Rev.* **117**, 7331–7376.
- Shukron, O., Seeber, A., Amitai, A., and Holcman, D. (2019). Advances using single-particle trajectories to reconstruct chromatin organization and dynamics. *Trends Genet.* **35**, 685–705.
- Sottile, F., Aulicino, F., Theka, I., and Cosma, M.P. (2016). Mesenchymal stem cells generate distinct functional hybrids in vitro via cell fusion or entosis. *Sci. Rep.* **6**, 36863.
- Starling, J.A., Maule, J., Hastie, N.D., and Allshire, R.C. (1990). Extensive telomere repeat arrays in mouse are hypervariable. *Nucleic Acids Res.* **18**, 6881–6888.
- Stewart, S.A., Dykxhoorn, D.M., Palliser, D., Mizuno, H., Yu, E.Y., An, D.S., Sabatini, D.M., Chen, I.S., Hahn, W.C., Sharp, P.A., et al. (2003). Lentivirus-delivered stable gene silencing by RNAi in primary cells. *RNA* **9**, 493–501.
- Stigter, D. (1977). Interactions of highly charged colloidal cylinders with applications to double-stranded. *Biopolymers* **16**, 1435–1448.
- Struhl, K., and Segal, E. (2013). Determinants of nucleosome positioning. *Nat. Struct. Mol. Biol.* **20**, 267–273.
- Sun, J., Zhang, Q., and Schlick, T. (2005). Electrostatic mechanism of nucleosomal array folding revealed by computer simulation. *Proc. Natl. Acad. Sci. USA* **102**, 8180–8185.
- Tarantino, N., Tinevez, J.Y., Crowell, E.F., Boisson, B., Henriques, R., Mhlanga, M., Agou, F., Israël, A., and Laplantine, E. (2014). TNF and IL-1 exhibit distinct ubiquitin requirements for inducing NEMO-IKK supramolecular structures. *J. Cell Biol.* **204**, 231–245.
- Tinevez, J.-Y., Perry, N., Schindelin, J., Hoopes, G.M., Reynolds, G.D., Laplantine, E., Bednarek, S.Y., Shorte, S.L., and Eliceiri, K.W. (2017). TrackMate: An open and extensible platform for single-particle tracking. *Methods* **115**, 80–90.
- Tokunaga, M., Imamoto, N., and Sakata-Sogawa, K. (2008). Highly inclined thin illumination enables clear single-molecule imaging in cells. *Nat. Methods* **5**, 159–161.
- Venkataramani, V., Herrmannsdörfer, F., Heilemann, M., and Kuner, T. (2016). SuReSim: simulating localization microscopy experiments from ground truth models. *Nat. Methods* **13**, 319–321.
- Verdaasdonk, J.S., Vasquez, P.A., Barry, R.M., Barry, T., Goodwin, S., Forest, M.G., and Bloom, K. (2013). Centromere tethering confines chromosome domains. *Mol. Cell* **52**, 819–831.
- Wieser, S., and Schütz, G.J. (2008). Tracking single molecules in the live cell plasma membrane—Do’s and Don’t’s. *Methods* **46**, 131–140.
- Woodcock, C.L., Skoultchi, A.I., and Fan, Y. (2006). Role of linker histone in chromatin structure and function: H1 stoichiometry and nucleosome repeat length. *Chromosome Res.* **14**, 17–25.
- Zeineddine, D., Hammoud, A.A., Mortada, M., and Boeuf, H. (2014). The Oct4 protein: more than a magic stemness marker. *Am. J. Stem Cells* **3**, 74–82.
- Zhang, Q., Beard, D.A., and Schlick, T. (2003). Constructing irregular surfaces to enclose macromolecular complexes for mesoscale modeling using the discrete surface charge optimization (DISCO) algorithm. *J. Comput. Chem.* **24**, 2063–2074.
- Zhao, Y., Wang, J., Liang, F., Liu, Y., Wang, Q., Zhang, H., Jiang, M., Zhang, Z., Zhao, W., Bao, Y., et al. (2019). NucMap: a database of genome-wide nucleosome positioning map across species. *Nucleic Acids Res.* **47** (D1), D163–D169.

STAR★METHODS

KEY RESOURCES TABLE

REAGENT or RESOURCE	SOURCE	IDENTIFIER
Chemicals, Peptides, and Recombinant Proteins		
JF549 HaloTag ligand	(Grimm et al., 2015)	N/A
Gelatin	Merck	Cat #ES-006-B
Hoechst 33342, Trihydrochloride, Trihydrate	Thermo Fisher	Cat #H1399
DMEM Medium	Thermo Fisher	Cat #15140122
GlutaMax	Thermo Fisher	Cat #35050061
Sodium pyruvate	Thermo Fisher	Cat #11360070
MEM non-essential amino acid	Thermo Fisher	Cat #11140050
2-Mercaptoethanol	Thermo Fisher	Cat #31350010
LIF ESGRO	Merck	Cat #ESG1107
Neurobasal	Thermo Fisher	Cat #21103-049
DMEM/F12	Thermo Fisher	Cat #21331020
B27	Thermo Fisher	Cat #17504044
N2	Thermo Fisher	Cat #17502048
Retinoic Acid	Sigma-Aldrich	Cat #R2625
Hygromycin	Thermo Fisher	Cat #10687010
PFA 4%	Alfa Aesar	Cat #43368
RNeasy Mini Kit	QIAGEN	Cat #74104
iScript cDNA Synthesis Kit	BIO-RAD	Cat #1708890
Lightcycler 480 SYBR green I master mix	Roche	Cat #4887352001
BCA Protein Assay Kit	Thermo Fisher Scientific	Cat #23227
Mini-PROTEAN TGX	Bio-Rad	Cat #4561084
Mouse anti-vinculin antibody	Sigma-Aldrich	Cat #V9131, RRID:AB_477629
Rabbit anti-HaloTag antibody	Promega	Cat #G9281, RRID:AB_713650
Rabbit anti-H2B antibody	Abcam	Cat #ab1790, RRID:AB_302612
Rabbit anti-H3 antibody	Abcam	Cat #ab1791, RRID:AB_302613
Sheep anti-Mouse IgG HRP-linked antibody	GE Healthcare	Cat #NA931, RRID:AB_772210
Donkey anti-Rabbit IgG HRP-linked antibody	GE Healthcare	Cat #NA934, RRID:AB_772206
Pierce ECL Western Blotting Substrate kit	Thermo Fisher Scientific	Cat #32106
Experimental Models: Cell Lines		
mESC H1tKO	Fan et al., 2005	N/A
mESC H2B-HaloTag	This paper	N/A
mESC H2B-HaloTag, TRF1-GFP	This paper	N/A
mESC H2B-HaloTag, Cenpa-GFP	This paper	N/A
mESC CTCF-HaloTag (A7 clone)	From Dr. Rafael Casellas (NIH, Bethesda)	N/A
mESC Oct4-HaloTag	This paper	N/A
mESC H2B-GFP	Sottile et al., 2016	N/A
Oligonucleotides		
Primer: Gapdh Forward: TCAAGAAGGTGGTGAAGCAGG	This paper	N/A
Primer: Gapdh Reverse: ACCAGGAAATGAGCTTGACAAA	This paper	N/A
Primer: Pou5f1 Forward: GTTGGAGAAGGTGGAACCAA	This paper	N/A
Primer: Pou5f1 Reverse: CTCCTTCTGCAGGGCTTTC	This paper	N/A
Primer: Nanog Forward: AACCAAAGGATGAAGTGCAAG	This paper	N/A
Primer: Nanog Reverse: TGAGCACAAACCCATCCTCCT	This paper	N/A
Primer: Sox1 Forward: CCTGTGGTTCTGCCTTTTGC	This paper	N/A

(Continued on next page)

Continued		
REAGENT or RESOURCE	SOURCE	IDENTIFIER
Primer: Sox1 Reverse: ACCAGGAAATGAGCTTGACAAA	This paper	N/A
Primer: Nestin Forward: TGGAAGTGGCTACATACAGGAC	This paper	N/A
Primer: Nestin Reverse: TCAGCTTGGGGTCAGGAAAG	This paper	N/A
sgRNA Oct4: AAGGTGGGCACCCCGAGCCGGGG	This paper	N/A
Cenpa ORF (NM_007681.3)	Genscript	Cat #OMu00596C
TRF1 ORF (NM_009352.3)	Genscript	Cat #OMu19848C
Recombinant DNA		
p1494_EF1a_H2B_Halotag	This paper	N/A
pLENTI_Cenpa_GFP	This paper	N/A
pLENTI_Trif1_GFP	This paper	N/A
pSNAP-H2B	New England Biolabs	Cat #N9179S
pFN205K HaloTag EF1a-neo Flexi	Promega	N/A
pLENTI-dCas9-VP64_GFP	Addgene (Konermann et al., 2015)	Cat#61422
p1494_EF1a_Hygro	Aulicino et al., 2014	N/A
pCMV-dR8.9 dvpr	Bob Weinberg (Stewart et al., 2003)	Addgene Cat #8455
pCMV-VSV-G	Bob Weinberg (Stewart et al., 2003)	Addgene Cat #8454
Software and Algorithms		
Fiji (ImageJ)	Schindelin et al., 2012	https://fiji.sc/
TrackMate	Tinevez et al., 2017	https://imagej.net/TrackMate
SMT_Motion_Classifier.m	This paper	https://github.com/PabloAu/Single-Molecule-Tracking-Analysis
MSD_Compare_Results.m	This paper	https://github.com/PabloAu/Single-Molecule-Tracking-Analysis
@msdanalyzer	Tarantino et al., 2014	https://tinevez.github.io/msdanalyzer/
NucMap	Zhao et al., 2019	https://bigd.big.ac.cn/nucmap/
Mesoscale chromatin modeling	Bascom et al., 2016; Perišić et al., 2010	N/A
Other		
N-STORM 4.0	Nikon Instruments	N/A
Cage incubator	Okolab	N/A
Andor iXon Ultra 897 EMCCD Camera	Oxford Instruments	N/A
CFI SR HP Apochromat TIRF 100x 1.49 oil objective	Nikon Instruments	N/A
Dual-View DV2	Photometrics	N/A
BD FACSAria II SORP cell sorter	Becton Dickinson	N/A
Lab-Tek I	Nunc	Cat #155411
TetraSpeck Microspheres	Thermo Fischer	Cat # T7279

RESOURCE AVAILABILITY

Lead Contact

Melike Lakadamyali (melikel@pennmedicine.upenn.edu) and Pia Cosma (pia.cosma@crg.eu).

Materials Availability

Plasmids and cell lines generated in this study are available upon request from the corresponding authors Melike Lakadamyali (melikel@pennmedicine.upenn.edu) and Maria Pia Cosma (pia.cosma@crg.eu).

Data and Code Availability

Data and codes are available upon request from the corresponding authors Melike Lakadamyali (melikel@pennmedicine.upenn.edu) and Maria Pia Cosma (pia.cosma@crg.eu).

EXPERIMENTAL MODEL AND SUBJECT DETAILS

Cell culture conditions and generation of cell lines

All mouse embryonic stem cells (mESC) were grown in a humidified incubator at 37°C - 5% CO₂ and were cultured on gelatin (#ES-006-B, Merck) coated plates, with serum Lif medium [DMEM, 15% FBS, 1% penicillin/streptomycin (#15140122, Thermo Fisher), 1% GlutaMax (#35050061, Thermo Fisher), 1% sodium pyruvate (#11360070, Thermo Fisher), 1% MEM non-essential amino acid (#11140050, Thermo Fisher), 0.2% 2-Mercaptoethanol (#31350010, Thermo Fisher), and 1000 U/ml LIF ESGRO (#ESG1107, Merck)].

Neural progenitor cells (NPCs) were generated by plating 44000 cells/cm² in gelatin coated Lab-Tek I (#155411, Nunc) chambers 24 hours prior to the start of differentiation. Cells were differentiated for 3 days in culture with Retinoic Acid containing medium (50% Neurobasal (#21103-049, Thermo Fisher), 50% DMEM/F12 (#21331020, Thermo Fisher), 1 × penicillin/streptomycin, 1 × GlutaMax, 2% B27 (#17504044, Thermo Fisher), 1% N2 (#17502048, Thermo Fisher), and 1 μM Retinoic Acid (#R2625, Sigma-Aldrich). Medium was changed every day. mESC H1tKO were a kind gift from Dr. Arthur Skoultchi (Fan et al., 2005). mESC CTCF_Halotag (A7 clone) were a kind gift from Dr. Rafael Casellas (NIH, Bethesda). mESC Halotag-Oct4 were generated by our collaborator Prof. Eran Meshorer (HUJI, Israel) by inserting Halotag sequence at the 5' of *endogenous Pou5f1* gene with CRISPR-Cas9, a single guide RNA (AAGGTGGGCACCCCGAGCCGGGG) and a donor vector carrying Halotag sequence flanked by *Pou5f1* 5' and 3' homology arms. mESC H2B-GFP were previously generated by lentiviral infection of mESC (Sottile et al., 2016).

Lentiviral vector HIV-H2B::mRFP was purchased from Addgene (# 18982). The PCR product derived from pH2B-eGFP (Addgene #11680) containing part of the H2B tagged with the eGFP was digested with EcoRI/Clal and subcloned into the lentiviral vector HIV-H2B::mRFP

mESC H2B-Halotag were generated by lentiviral infection of mESC (GS1 129Sv) and mESC H1tKO (Fan et al., 2005) with a lentiviral plasmid encoding for H2B_Halotag under EF1a promoter (p1494_EF1a_H2B_Halotag) following The RNAi Consortium (TRC) low throughput viral production protocol (<https://portals.broadinstitute.org/gpp/public/resources/protocols>). Transduced cells were selected for hygromycin resistance (#10687010, Thermo Fisher). Cells expressed H2B-Halotag at levels comparable or lower than endogenous H2B.

mESC H2B_Halotag + Cenpa_GFP or + Trf1_GFP were generated by lentiviral infection of mESC H2B_Halotag cells with pLenti_Cenpa_GFP or pLenti_Trif1_GFP as described above. Transduced cells were selected by cell sorting of GFP positive cells (FACS Aria) 96 h post transduction. Lentiviral vector expressing C-terminally Halo-tagged H2B was generated by Gibson cloning by preamplifying Halotag from pFN205K HaloTag EF1a-neo Flexi (Promega) and H2B from pSNAP-H2B (#N9179S, New England Biolabs) and cloning them into p1494 plasmid with Hygromycin resistance and EF1a promoter.

Lentiviral vectors expressing C-terminally eGFP-tagged Cenpa and Trf1 under EF1a promoter were generated by Genscript custom gene service by subcloning Cenpa ORF (#OMu00596C, NM_007681.3) and Trf1 ORF (#OMu19848C, NM_009352.3) into pLenti-dCas9-VP64_GFP backbone (Konermann et al., 2015).

METHOD DETAILS

Cell Labeling for Single Molecule Tracking Imaging

For SMT experiments in mESC, cells were plated at a 31000 cells/cm² density in Lab-TekI chambers 24 hours before imaging. For SMT experiments in NPCs, cells were differentiated as described above and imaged after 3 days of differentiation. Cells were labeled with 2 pM and 5 pM of JF549-Halotag ligand (kind gift from Dr. Luke Lavis) diluted in grow or differentiating medium. Cells were incubated in presence of the dye for 30 min in the incubator and subsequently washed once in Phenol red free medium with Hoechst (1:1000 dilution) for 15 min in the incubator. Cells were finally washed once with Phenol red free medium for 5 min in the incubator. For SMT imaging of living cells, cells were kept in Phenol Red free grow or differentiation medium. For SMT imaging of fixed cells, right after labeling, samples were fixed for 10 min at RT in PFA 4% (#43368, Alfa Aesar), diluted in PBS, and washed 3 times in PBS. JF549-Halo ligand diluted in phenol red free resting medium for 30 min in the incubator. Cells were washed once for 15 min in the incubator with fresh medium and then once for 5 min. JF labeled ligands were kindly provided by Dr. Luke Lavis (Janelia Research Campus). For FRAP experiments, mESC H2B-Halo cells were incubated for 30 minutes with JF549-Halo fluorophore and washed twice in Phenol red free medium.

Imaging

Imaging was performed in an N-STORM 4.0 microscope (Nikon Instruments) equipped with an Okolab cage incubator system set at 37°C, 5% CO₂ and controlled humidity. Images were taken with a 100X 1.49 oil objective and an EMCCD camera Andor iXon Ultra 897 (Oxford Instruments). This combination provides an effective pixel size of 160 nm. We used HILO illumination (Tokunaga et al., 2008) and a quad-band beam splitter ZT405/488/561/640rpc (Chroma Technology Corporation). The Perfect Focus System (PFS) equipped on the NSTORM microscope was used during the acquisition.

Two imaging conditions were set to measure separately fast and slow dynamics. The fast dynamics experiments were performed with 15 ms of camera exposure time, a 561 nm laser power of ~200 W/cm² and 10 pM concentration of JF-549-Halo fluorophore in

the labeling step. For the slow dynamics we used 500 ms of camera exposure time, a 561 nm laser power of ~ 25 W/cm² and 4 pM concentration of JF-549-Halo fluorophore. For the fast SMT at 15 ms, we acquired 3000 frames (45 s), and for slow SMT videos at 500 ms of exposure time, 600 frames (5 minutes).

Apart from the JF, Hoechst 33342 was used for staining chromatin. This allows to identify regions of more condensed chromatin and to precisely segment each cell nucleus subROI. In both cases, we imaged four frames of Hoechst 33342 at the end of each SMT video, using the 405 nm laser at a very low power (~ 5 W/cm²) with 2 s of camera exposure time. In order to classify the trajectories as euchromatic or heterochromatic, the sub regions were defined by manually drawing subROIs based on Hoechst 33342 fluorescence intensity, which correlates with chromatin compaction. In addition, a brightfield image of each FOV was taken before and after the imaging procedure to control for apparent cell displacement or cell dead during the experiment. Cells were imaged on their corresponding phenol red free resting medium.

2-Color Imaging

A Dual-view system based on a dichroic mirror was used for the 2-Color SMT experiments. The camera was splitted in two FOVs of 256x256 pixels (40x40 μ m) each.

A calibration with fluorescent TetraSpeck Microspheres (Thermo Fisher Scientific) was performed before and after the experiments to align both channels with a precision below 10 nm. A second order 2D polynomial transform function was calculated from the beads localizations of both channels (Otterstrom et al., 2019). Then the alignment of the trajectories on both channels was performed by using a linear affine transformation.

The H2B trajectories were divided in two groups based on their overlapping with Telomere trajectories. To do so, a maximum spatial distance of 250 nm between the positions of both trajectories (Telomeres and H2B) was set to identify telomeric H2B. Note that both trajectories should overlap also in time, meaning that they are present on the same frame.

Tracking

TrackMate (Tinevez et al., 2017) was used for localization and tracking of the single molecules. For the localization step, we used the LoG detector with sub-pixel localization enabled and for the tracking step, the Simple LAP tracker with a maximum frame gap of 2 frames.

The images were segmented by manually selecting the nuclear areas from Hoechst 33342 signal, corresponding to each cell nucleus. We performed this tracking procedure on each individual nucleus separately.

Different input parameters were used for each imaging condition. The intensity threshold for the localizations was defined to minimize false localizations: 150 for the 500 ms data, and 70 for the 15 ms data. In both cases the Linking max distance was set to 400 nm and the gap-closing max distance to 200 nm. The estimated blob diameter of the diffraction-limited spot was set to 800 nm (5 pixels). The lists of trajectories were saved as an xml file for their analysis.

Trajectory Analysis

The trajectories were analyzed using a custom written MATLAB code that makes use of some functions from @msdalyzer (Tarrantino et al., 2014). First, it filters the trajectories based on their track length. For the analysis of the trajectories from 15 ms exposure time, only those tracks longer than 4 frames were analyzed. For the 500ms data, all the trajectories were analyzed, and 1 frame localizations were considered to be binding events lasting 500 ms. Then, it classifies the trajectories in different motion types. After having the subgroups, the code computes quantitative analysis on the trajectories for extracting multiple measures. And finally, it compares the results from the different cell conditions.

The MSD curves were obtained as a time average from the trajectories (T-MSD), assuming that the displacements at different times are equivalent fulfilling the ergodic principle (Manzo et al., 2015):

$$TMSD = \frac{1}{N-m} \cdot \sum_{i=1}^{N-m} (x_j(t_i + m \cdot t_{lag}) - x_j(t_i))^2$$

The time ensemble average of the MSD (TE-MSD) is the average of the T-MSD computed on all the trajectories for a particular condition:

$$TEMSD = \frac{1}{T} \frac{1}{N-m} \cdot \sum_{j=1}^T \sum_{i=1}^{N-m} (x_j(t_i + m \cdot t_{lag}) - x_j(t_i))^2$$

Where t_{lag} is the exposure time of the experiment, in our case 15ms.

TEMSD was plotted as a discrete bar plot showing the average and standard deviation for each time lag point (Figure 3C).

Trajectory Classification

The trajectories were classified into two different subgroups based on their motion type: Confined and Brownian/Directed. This was done by fitting a power law function to each individual TMSD curve (Manzo and Garcia-Parajo, 2015):

$$TMSD = 4 \cdot D \cdot t_{lag}^{\alpha}$$

where D is the diffusion coefficient and t_{lag} is the time lag between the different time points of the track. α is called the anomalous coefficient. Trajectories with $\alpha < 1$ were considered as Confined and with $\alpha \geq 1$ as Brownian/Directed.

In addition, a third group of trajectories performing both confined motion and free diffusion were identified and separated. First, we iterate through all the trajectories searching for frame-to-frame jumps that are bigger than the mean frame-to-frame jump of the track plus a spatial threshold multiplied by the standard deviation of the frame to frame jump of the track. We used 1.5 for that spatial threshold. In addition, the total distance traveled by butterfly trajectories must be bigger than a distance threshold multiplied by the mean frame to frame jump of the track. We used 8 for that distance threshold. Once identified, the butterfly trajectories were segmented into their multiple Confined and Brownian/Directed parts based on their geometrical properties. A Brownian/Directed segment must fulfill the condition that a minimum percentage of its points lie outside the polygon (convex hull) formed by the points of previous and posterior segments of the trajectory. We used a minimum percentage of outside points of 30%. Also, we imposed a minimum linearity to the Directed/Brownian segments. Linearity was calculated by dividing the distance between the first and last point of a certain segment by the sum of displacements of all the individual jumps of that segment. We iterate using segments of 3 points and used a linearity ratio threshold of 0.8.

Diffusion Coefficients

For an accurate calculation of the diffusion coefficient of the confined trajectories, only the first 3 points of each T-MSD curve corresponding to each trajectory were fitted with linear distribution (Michalet, 2010; Michalet and Berglund, 2012):

$$TMSD = 4 \cdot D \cdot t_{lag} + offset$$

A threshold on the coefficient of determination $R^2 \geq 0.8$ was set to filter out the bad fits. Since the distribution of the diffusion coefficients (D) follows a log-normal distribution (Nandi et al., 2012), the $\text{Log}_{10}(D)$ was used for a proper visualization of the different subpopulations of trajectories. Consequently, a Gaussian Bi-modal distribution was fit of that $\text{Log}_{10}(D)$ distribution.

Circle Confined Diffusion Model

The radius of confinement of the whole population of trajectories was estimated by fitting a confined circle diffusion model to the time ensemble of the confined trajectories (Wieser and Schütz, 2008):

$$TEMSD = R^2 \cdot \left(1 - e^{-\frac{4 \cdot D_{micro} \cdot t_{lag}}{R^2}} \right) + O$$

where R is the radius of confinement and D_{micro} the diffusion coefficient at short timescales. O is an offset value that comes from the localization precision limit of SMLM techniques. In this case, we have estimated a localization precision of around 40 nm from the experimental data. We used a nonlinear fitting with least-squares.

Residence Times

The residence times of H2B bound to chromatin were extracted from the 500 ms data, which measures chromatin dynamics on a higher timescale. In this case, all the trajectories were analyzed, considering that a one-frame localization is a binding event which has a residence time of 500 ms. The dissociation kinetics were estimated from the track length of each individual trajectory. First the track duration distribution is transformed into the survival fraction of molecules defined by $1 - \text{Cumulative Distribution Function}$ of the track lengths (1-CDF). Then, we fit a two-component exponential decay function to the survival fraction (Ball et al., 2016; Chen et al., 2014; Mazza et al., 2012):

$$F(t) = f \cdot e^{-k_1 \cdot t} + (1 - f) \cdot e^{-k_2 \cdot t}$$

Where f is the fraction belonging to each population, k_1 the short-live component associated with unspecific chromatin binding and k_2 the long-live component associated with specific chromatin binding.

In addition, a photobleaching correction was performed by fitting a double exponential to the evolution of the number of localizations over time during the experiment (Chen et al., 2014).

$$N(t) = f_b \cdot e^{-k_{b1} \cdot t} + (1 - f_b) \cdot e^{-k_{b2} \cdot t}$$

Then, the corrected residence times are obtained from the following relation:

$$k_{measured} = k_{corrected} + k_{bleaching}$$

where $k_{measured}$ is the dissociation rate constant estimated directly from the experimental data, $k_{bleaching}$ (i.e., k_{b2} in the double exponential) is the photobleaching kinetics constant, and $k_{corrected}$ is the dissociation rate constant after correction. Note that k is in s^{-1} units and the residence times are inversely proportional.

For a further control, fixed cells were imaged under the same experimental conditions, obtaining similar values for the different cell types, which were larger than those of live cells, assuring that measured residence times are related with protein instability due to live cell activity.

Mesoscale Modeling of mESC and mNPC Chromatin Fibers

To simulate fibers representative of chromatin in mouse embryonic stem cells (mESCs) and neuronal progenitor cells (mNPCs), we analyzed publicly available data to determine nucleosome positions, linker histone (LH) density, and histone-core tail acetylation levels. We consider the *Pou5f1* gene, known for being upregulated in non-differentiated cells. We simulated the region of Chr17 spanning 35626358 bp to 35657661 bp (mm9 reference). It corresponds to a chromatin fiber length of ~31 kbp and contains 121 nucleosomes in mESC and 151 nucleosomes in mNPC.

Nucleosome positions were obtained from the database NucMap (Zhao et al., 2019), that includes the analysis of 798 experimental MNase-Seq data from 477 samples across 15 species. We used the nucleosome positions obtained with the DANPOS algorithm (Chen et al., 2013) on the MNase-Seq data of mESC and mNPC reported by Mieczkowski et al. (2016). In particular, NucMap uses the DANPOS version 2.1.4 with default parameters; P value cutoff for defining a peak is set to $1e-10$, minimal tail-to-head distance between neighboring peaks to 40 bp, and minimal width of each peak to 40 bp (<https://sites.google.com/site/danposdoc/home/dpeak/parameters>). The list of linker lengths and nucleosome free regions (NFRs) for each system can be found in the Supplementary Information excel file (Table S1). LH density was set to 0.5 LH per nucleosome for the mESC fibers, and to 0.8 LH per nucleosome for the mNPC fibers, as reported previously by Skoutchi and coworkers (Fan et al., 2003, 2005). The LHs were distributed uniformly to fulfill these densities. That means 1 LH every 2 nucleosomes, and 4 LHs every 5 nucleosomes for mESC and mNPC, respectively. Based on immunofluorescence data (Figure S1C), the concentration of histone core tail acetylation of H3 and H4 was set to 10% for the mNPC systems and 15% for the mESC systems to reproduce the 1.5 ratio of acetylation levels in mESC versus mNPC. Since histone acetylation are distributed in clusters (Roh et al., 2007), we distributed the acetylated nucleosomes in both systems in two islands of similar size before and after the gene of interest. Specific positions of acetylation can be found in the Supplementary file (Table S1) (also shown in Figure S1B for one of the islands).

The starting configuration of each fiber (Figure S1B) corresponds to the ideal zigzag conformation oriented with the fiber axis parallel to the z axis, as we have shown this conformation to be the lowest energy (Sun et al., 2005). We use our mesoscale chromatin model (Figure S1A) to simulate 30 independent trajectories of 80 million Monte Carlo (MC) steps for the *Pou5f1* system. To define these trajectories, we used different initial random number seeds and a different DNA twist value of -12° , 0° , or $+12^\circ$ to mimic natural variations in the B-DNA twist (Drew and Travers, 1985). The last 10 million steps of each trajectory were used for analysis, with a sampling frequency to yield 3000 configurations. Briefly, our model combines nucleosomes, histone core tails, linker DNA, and linker histone by coarse-grained units at different levels of resolution to create oligonucleosome fibers. The model has evolved over 18 years and validated against growing experimental data (Arya and Schlick, 2009; Arya et al., 2006; Bascom and Schlick, 2018; Portillo-Ledesma and Schlick, 2020a). The nucleosome core with wrapped DNA and without tails is treated as an electrostatic charged object, coarse grained from the crystal structure of the nucleosome core particle at 1.9 Å resolution (Davey et al., 2002); its surface is represented with 300 Debye-Hückel pseudo-charges computed by our DISCO algorithm to approximate the electric field of the atomistic nucleosome obtained by the Poisson Boltzmann formulation (Zhang et al., 2003). Flexible histone core tails are coarse grained with the Levitt-Warshel united-atom bead model (Levitt and Warshel, 1975) as 1 bead per 5 amino acids, and each bead charge is calculated by the DISCO algorithm (Arya and Schlick, 2006). Folded histone tails, mimicking acetylated tails, are modeled with increased stretching, bending, and torsional force constants by a factor of 100 (Colleparado-Guevara et al., 2015). Linker DNA connecting nucleosomes is modeled by a combined wormlike-chain and bead model with a resolution of ~9 bp (Jian et al., 1997) and salt-concentration dependent charges determined with the Stigter method (Stigter, 1977). Finally, linker histone H1E is coarse grained similar to histone tails with the Levitt-Warshel united-atom bead model and with charges calculated with DISCO (Luque et al., 2014). The globular head is modeled with 6 beads and the C-terminal domain with 22 beads; the N-terminal domain is neglected since it has minor role in chromatin organization.

Standard energy terms and various local and global MC sampling moves are used to improve the conformational sampling. The total energy function contains stretching terms for linker DNA, histone tails, and linker histone that maintain equilibrium distances; bending terms for linker DNA, histone tails, and linker histone; twisting terms for linker DNA; electrostatic Debye-Hückel terms to represent all charge-charge interactions within chromatin; and excluded volume terms for all beads, described with a Lennard-Jones potential. The MC moves include local translation, local rotation, and global pivot rotations for linker DNA beads or nucleosomes, and a regrowth for histone tails (Arya and Schlick, 2009). Acceptance of the first three moves is based on the regular Metropolis criteria (Metropolis and Ulam, 1949) while acceptance of the tail regrowth move is made according to the Rosenbluth criteria (Rosenbluth and Rosenbluth, 1955). Full details concerning the energy terms, parameter values, and sampling can be found in Arya and Schlick (2009) and in Bascom and Schlick (2018).

Convergence of the systems is monitored by determining the evolution along the trajectory of global variables like the sedimentation coefficient and the root mean squared deviation of the nucleosomes with respect to the initial structure, and by monitoring local variables like the distance between the first and last nucleosome and evolution of angles formed by three adjacent (in sequence) nucleosomes.

Chromatin Structure Analysis of Coarse-Grained Model

The sedimentation coefficient ($S_{w,20}$), in units of Svedbergs, is used to describe the compaction of the fiber. It is defined by the expression:

$$S_{w,20} = ((S_1 - S_0) * LH_{conc} + S_0) * \left(1 + \left(\frac{R_1}{N_C} \right) \sum_i \sum_j \frac{1}{R_{ij}} \right),$$

where S_0 is the sedimentation coefficient for a mononucleosome with LH bound (12 S) (Butler and Thomas, 1998), S_1 is the sedimentation coefficient for a mononucleosome without LH (11.1 S) (Garcia-Ramirez et al., 1992), LH_{conc} the concentration of LH in the fiber, R_1 the spherical radius of a nucleosome (5.5 nm), N_C the number of nucleosomes in the fiber, and R_{ij} the distance between two nucleosomes i and j .

The radius of gyration, which describes the overall dimension of the polymer chain, is measured as the root mean squared distance of each nucleosome from the center of mass according to the relation:

$$R_g^2 = \frac{1}{N_C} \sum_{j=1}^N (r_j - r_{mean})^2$$

where N_C is the number of nucleosomes, r_j the center position of the nucleosome core j , and r_{mean} the average of all core positions (Perišić et al., 2010).

Fiber volumes are calculated using the AlphaShape function of MATLAB, which creates a nonconvex bounding volume that envelops the nucleosomes. Surfaces are visually inspected to ensure that they represent correctly the fiber morphology. This is because non cylindrical-like shapes may not well be estimated. In that case, the AlphaShape object can be manipulated to tighten or loosen the fit around the points to create a nonconvex region.

Packing ratio is used to describe the compaction of the fiber and is measured as the number of nucleosomes contained in 11 nm of fiber. It is determined according to the relation:

$$Packing\ ratio = \frac{11 \cdot N_C}{fiber_length}$$

where N_C is the number of nucleosomes and the fiber length is calculated using a cubic smoothing spline function native from MATLAB.

Nucleosome clusters are quantified by determining the average number of nucleosomes per cluster and average number of clusters using the Density-based clustering algorithm DBSCAN (Sander et al., 1998), as implemented in MATLAB. DBSCAN is designed to discover clusters in noisy data by partitioning the observations (the n -by- n internucleosome distance matrix) into clusters.

The algorithm identifies three kinds of points: core, border, and noise points, based on a threshold for a neighborhood search radius (epsilon) and a minimum number of neighbors in the given neighborhood (*minpts*). Any point x in the dataset with a neighbor count greater than or equal to *minpts* is selected as a core point. Alternatively, if the number of neighbors is less than *minpts*, but the point x belongs to an epsilon neighborhood of some core point z , the point is identified as a border point. Finally, if a point is neither a core nor a border point, it is identified as a noise point and not assigned to any cluster.

The algorithm is implemented as follows:

1. From the input dataset, select the observation x_1 and assign it to cluster 1.
2. Find the set of points within the epsilon neighborhood of the current point.
 - a. If the number of neighbors is less than *minpts*, label the current point as noise. Go to step 3.
 - b. Otherwise, label the current point as a core point belonging to cluster 1.
3. Iterate over each neighbor (new current point), and repeat step 2 until no new neighbors that can be labeled as belonging to the current cluster are found.
4. Select the next observation x_2 as the current point and increase the cluster count by 1.
5. Repeat steps 2-4 until all points in the input dataset are assigned.

If the distance between two border points belonging to different clusters is smaller than epsilon, DBSCAN merges the two clusters into one. The *minpts* and epsilon parameters were chosen based on the heuristic provided by the algorithm developers (Ester et al., 1996). *Minpts* was selected as 3 nucleosomes as it is recommended to be at least $\geq D + 1$, where D is the number of dimensions in the dataset. However, this parameter does not significantly affect the overall results of the clustering (Ester et al., 1996). The radius, epsilon, was selected as 20 nm based on the fiber dimensions.

Gene Expression Analysis

RNA from ESCs and NPCs cells was extracted with RNeasy Mini Kit (#74104, QIAGEN). Reverse transcription was carried out with iScript cDNA Synthesis Kit (#1708890, BIO-RAD). qPCR was performed with the primers listed below and Lightcycler 480 SYBR green I master mix (#4887352001, Roche), plates were run on a Lightcycler 480 (Roche) qPCR instrument.

qPCR Primer list:

	Forward	Reverse
Gapdh	TCAAGAAGGTGGTGAAGCAGG	ACCAGGAAATGAGCTTGACAAA
Pou5f1	GTTGGAGAAGGTGGAACCAA	CTCCTTCTGCAGGGCTTTC
Nanog	AACCAAAGGATGAAGTGCAAG	TCCAAGTTGGGTTGGTCCAAG
Sox1	CCTGTGGTTCTGCCTTTTGC	TGAGCACAAACCCATCCTCCT
Nestin	TGGAAGTGGCTACATACAGGAC	TCAGCTTGGGGTCAGGAAAG

Protein Extraction and Western Blot

H2B-HaloTag and H2B-GFP ESC cells were harvested by scraping and processed as previously described (Berlinger et al., 2016). Protein extracts were quantified with BCA Protein Assay Kit (#23227, Thermo Fisher Scientific). Protein extracts were loaded on 4%–15% precast protein gels (#4561084, Mini-PROTEAN TGX, Bio-Rad). Membranes were incubated with mouse anti-vinculin 1:1000 (#V9131, Sigma-Aldrich), rabbit anti-HaloTag 1:500 (#G9281, Promega), rabbit anti-H2B 1:5000 (#ab1790, Abcam) and rabbit anti-H3 1:5000 (#ab1791, Abcam) and with secondary antibodies sheep anti-Mouse IgG HRP-linked 1:1000 (#NA931, GE Healthcare) and Donkey anti-Rabbit IgG HRP-linked 1:2000 (#NA934, GE Healthcare). HRP-derived signal was detected with Pierce ECL Western Blotting Substrate kit (#32106, Thermo Fisher Scientific) on an Amersham Imager 600 (#29083461, GE Healthcare Life Sciences).

Contact Probability Matrices

Nucleosome contact matrices describe the fraction of MC steps that the core, histone tails, or linker DNA of a nucleosome i are in contact (within 2 nm) with any of these elements of a nucleosome j . For a single fiber contact map, contacts are counted along the corresponding trajectory and normalized by the maximum number of contacts across all frames to determine the probabilities, which are then plotted in logarithmic scale. For the contact matrices of the 30-trajectory ensemble, all probabilities of each independent trajectory are summed before plotting.

Contact probability matrices are used to characterize fiber internal folding motifs. Specific fold patterns can be identified by the density features (Grigoryev et al., 2016). Local inter-nucleosome interactions ($i \pm 2, 3$), corresponding to the canonical zigzag topology, locate near the diagonal of the matrices; medium-range interactions ($i \pm 4, 5, 6$) indicative of hairpin- and sharp kinks-type folds are evidenced by regions perpendicular to the main diagonal; and long-range contacts ($i \pm 7, > 7$), indicative of hierarchical looping, are evidenced by regions parallel to the main diagonal.

Zigzag Geometry Inside the Clutches

For representative trajectories of mESC and mNPC, we studied the zigzag geometry inside the clutches. Specifically, we calculated for consecutive nucleosomes (bonded) belonging to the same clutch the probability distribution of the dimer distance, distance between two consecutive nucleosomes (nucleosome i and nucleosome $i+1$); the triplet angle, angle formed by three consecutive nucleosomes (nucleosome i , nucleosome $i+1$, and nucleosome $i+2$); and the dihedral angle, angle between two planes about nucleosomes $i+1$ and $i+2$ defined by four consecutive nucleosomes (nucleosome i , $i+1$, $i+2$, and $i+3$). As we are interested in the zigzag geometry, consecutive nucleosomes belonging to the same clutch but connected by a nucleosome free region instead of a typical linker DNA were not considered in the statistics.

SMLM Image Generation

We used SuReSim software for the generation of synthetic SMLM images (Venkataramani et al., 2016). We imported the final 3D nucleosome positions of each fiber obtained from the mesoscale chromatin modeling to SuReSim and generated a list of x - y - z positions of fluorophore labeled nucleosomes taking into account fluorophore blinking and precision in determining each fluorophore's position. We input a discrete list with the 3D coordinates of the nucleosome centers obtained from the mesoscale computational model. We generate the images using realistic parameters that resemble the experimental conditions (Ricci et al., 2015). We used a localization precision of 10 nm, an epitope length of 10 nm with a random 3D angle distribution with standard deviation of 50° , a labeling efficiency of 75%, a localization efficiency of 80%, and a ratio of 2 fluorophores per antibody. We simulated 10,000 frames in order to obtain a number of localizations per cluster in the same range as in our experimental measurements.

We performed 1000 random 3D projections of the localizations using a custom-written MATLAB code. Then we projected those images in 2D, taking into account that a maximum slice of 400 nm will be detected by the microscope.

Cluster Analysis

For cluster quantification, we used a previously described method (Ricci et al., 2015). The localization lists were binned to construct discrete localization images with pixel size of 10 nm. These were convoluted with a 5x5 pixels kernel to obtain density maps and transformed into binary images by applying a constant threshold, such that each pixel has a value of either 1 if the density surpasses the threshold value and 0 if not. We used a threshold of 0.008 localizations/nm². The x - y coordinates in the binary image were grouped into clusters using a distance-based algorithm. Cluster sizes were calculated as the standard deviation of x - y coordinates from the

centroid of the cluster. In addition, we used an estimated localization precision of 10 nm and a minimum number of molecules so that a group is considered a clutch of 10 localizations.

The synthetic super resolution images of the fibers were rendered using a custom-written software (Insight3, provided by Bo Huang, University of California).

QUANTIFICATION AND STATISTICAL ANALYSIS

Statistical analysis was performed in GraphPad PRISM 5 and custom MATLAB codes. Statistical parameters including the sample size (N), the mean and the standard deviation are reported in the corresponding figures and figure legends. When a measure is obtained by fitting a model, the estimated value with the 95% confidence interval is reported.